Interplay of Bandstructure and Quantum Interference in Multiwall Carbon Nanotubes

Dissertation
zur Erlangung des Doktorgrades der Naturwissenschaften
(Dr. rer. nat.)
der naturwissenschaftlichen Fakultät II – Physik
der Universität Regensburg

vorgelegt von
Bernhard Stojetz
aus Vilshofen

Dezember 2004

Die Arbeit wurde von Prof. Dr. Ch. Strunk angeleitet.
Das Promotionsgesuch wurde am 22. 12. 2004 eingereicht.
Das Kolloquium fand am 10. 2. 2005 statt.

Prüfungsausschuss:	Vorsitzender:	Prof. Dr. Ch. Back
	1. Gutachter:	Prof. Dr. Ch. Strunk
	2. Gutachter:	Prof. Dr. M. Grifoni
	weiterer Prüfer:	Prof. Dr. M. Maier

I found it hard
Its hard to find
Oh well, whatever,
Nevermind

Kurt Cobain

Contents

Chapter 1

Introduction

Metallic wires as used in standard microelectronic devices nowadays allow to be fabricated with widths and heights of several tens of nanometers. Despite these small dimensions, their electronic transport properties can be understood to a large extent in terms of classical diffusive motion.
Recently, metallic contacts could be attached also to single molecules [1]. In contrast to diffusive metal wires, molecules are well defined systems, both with respect to their atomic structure and their electronic conduction properties: all molecules of a given structure are identical on atomic scale, and electronic transport through a single molecule is determined solely by it's overall, coherent wavefunction.
Since their discovery in 1991, multiwall carbon nanotubes (MWNTs) take an intermediate position between the world of identical molecules and disordered solids. [2]. On one hand, they can be considered as a set of seamlessly rolled up graphene sheets (referred to as 'shells'), which are put one into another. With this respect, they have to be classified as perfect molecules.
On the other hand, their typical length of several micrometers and diameters up to 50 nm exceed by far the dimensions of most other molecular systems. Their large size allows the occurrence of imperfections of the atomic structure, without turning the molecule into a completely different one, what would be the case for smaller systems. Such imperfections are for example introduced by atomic displacements and adsorbates on the outermost nanotube shell. In this sense MWNTs represent a disordered molecular system, in which electronic transport is influenced both by the molecular wavefunctions and the imperfections of the atomic structure.
In the last years, large effort has been made in order to clarify and characterize the transport properties of MWNTs (for an overview see Ref. [3]). One main reason for that is the fundamental interest in electronic transport on a molecular scale, which is most easily accessed with MWNTs. Furthermore, also a variety of microelectronic

devices bear the perspective of being assembled by nanotubes, either completely or by using the tubes as connection wires [4, 5].
Despite the large efforts, the electronic properties of MWNTs could not be clarified to a satisfying extent. For example, the interaction of adjacent nanotube shells is not clear, since in the measurement only the outermost shell is contacted. Here, the question arises, to which extent electric current is carried also by the inner shells [6].
Thus, the main goal of this thesis is to shed some more light on transport in MWNTs. Especially the question of a possible interplay between the molecular structure and the disorder is addressed, as well as the resulting consequences for the electronic transport.
Experimentally, the main investigation tool in this work are conductance measurements on single MWNTs at low temperatures and high magnetic fields. A very efficient gate is used for a considerable variation of the nanotube's Fermi level. The results are compared to numerical tight-binding calculations, as performed by our collaborators S. Roche and F. Triozon [7].
The thesis is organized as follows: A review of the electronic bandstructure within the tight binding approach is given in Chapter 2. The tight-binding method represents a very efficient and successful tool for a basic understanding of the conduction properties of carbon nanotubes. Furthermore, it allows a comparatively easy inclusion of magnetic fields and disorder.
Subsequently, several mesoscopic transport effects are described, which are observed in MWNTs (Chapter 3). Here only those effects are considered, which are crucial for the interpretation of the measurements in this work.
After an overview on the sample-fabrication methods and the measurement setup (Chapter 4), the first experimental results are presented (Chapter 5). These results serve as a motivation for more extensive investigations, which are presented and discussed in the following sections.
In Chapter 6, the intricate interplay between the electronic bandstructure and the disorder of the system is addressed. This is done by means of magnetoconductance measurements, where the Fermi level in the nanotube is changed within a large range by means of a highly efficient backgate. The latter offers the possibility of tuning the Fermi level across several nanotube subbands, which in turn strongly affects the conduction properties.
Finally, Chapter 7 is concerned with the conduction properties of MWNTs with large diameters of about 30 nm. If for such tubes the magnetic field is aligned with the tube axis, it's cylindrical shape is predicted to cause a variety of effects in the conductance. All of these effects are closely related to the fundamental Aharonov-Bohm effect [8], which predicts conductance oscillations of a ring-shaped conductor

as a function of the magnetic flux through the surface enclosed by the ring. The predictions are investigated again by magnetotransport measurements.
For nanotubes of large diameter in perpendicular fields, there exist several contradictory theoretical models, predicting the occurence of Landau levels and conductance oscillations. Thus, in the last section of Chapter 7 corresponding measurements are reported and compared to numerical calculations.

Chapter 2

Electronic Bandstructure of Carbon Nanotubes

The electronic bandstructure of perfect, i.e. defect-free and infinitely long single wall carbon nanotube can be derived from that of a single layer of graphite, or a graphene. Therefore, first the electronic structure of graphene will be reviewed, which will be specialized afterwards to carbon nanotubes in a magnetic field. This section is mainly inspired by the book of R. Saito *et al.* [9].

2.1 Graphene

The carbon atoms in a graphene sheet form a planar hexagonal lattice. In real space, the unit vectors of the sheet are given by

$$\mathbf{a}_1 = \left(\frac{\sqrt{3}}{2}a, \frac{a}{2}\right), \ \mathbf{a}_2 = \left(\frac{\sqrt{3}}{2}a, -\frac{a}{2}\right), \tag{2.1}$$

with a lattice constant of $a = |\mathbf{a}_1| = |\mathbf{a}_2| = 2.46$Å. The corresponding reciprocal lattice is spanned by the vectors

$$\mathbf{b}_1 = \left(\frac{2\pi}{\sqrt{3}a}, \frac{2\pi}{a}\right), \ \mathbf{b}_2 = \left(\frac{2\pi}{\sqrt{3}a}, -\frac{2\pi}{a}\right). \tag{2.2}$$

Each unit cell contains two carbon atoms and can hence accomodate two valence electrons. It has the shape of a rhomb, while the first Brillouin zone forms a hexagon, as shown in Fig. 2.1.

For each carbon atom, three σ bonds hybridize in a sp^2 configuration. The fourth valence electron remains in an atomic p_z state , perpendicular to the sheet, and hybridizes with all other p_z-orbitals to form a delocalized π-band. Only this, covalent,

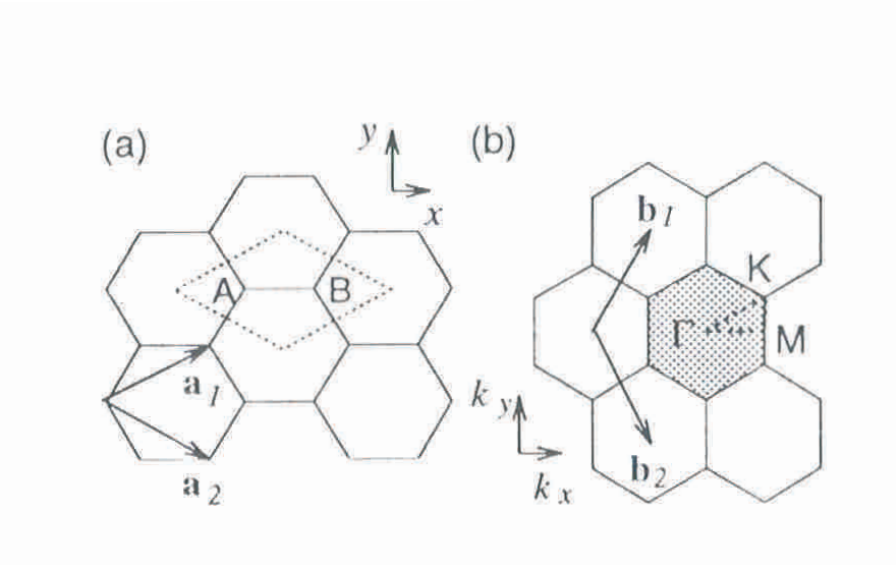

Figure 2.1: (A) Direct graphene lattice with primitive vectors $\mathbf{a}_1$ and $\mathbf{a}_2$.The rhomb-shaped primitive cell contains two carbon atoms, denoted A and B. (B) Corresponding reciprocal lattice (spanned by $\mathbf{b}_1$ and $\mathbf{b}_2$). The grey shaded region marks the first Brillouin zone. The positions of some high-symmetry points (Γ, K, M) are depicted. (Figure adapted from Ref. [9]).

π-band is considered for the bandstructure calculation, since it turned out to be most important for determining the solid state properties of graphite.

2.2 Tight Binding Method for Graphene

The tight-binding scheme allows to calculate the π-electron bands of graphene. As an ansatz, Bloch functions serve, as given by

$$\Phi_j(\mathbf{k},\mathbf{r}) = \frac{1}{\sqrt{N}} \sum_{\mathbf{R}_\alpha} e^{i\mathbf{k}\cdot\mathbf{R}_\alpha} \varphi_j(\mathbf{r}-\mathbf{R}_\alpha),\ j = 1...n,\ \alpha = A, B \tag{2.3}$$

where n denotes the number of atomic eigenfunctions per unit cell, $\mathbf{R}_\alpha$ are the positions of the inequivalent carbon atoms A and B in the unit cell and $\varphi_j(\mathbf{r}-\mathbf{R}_\alpha)$ is the $2p$-wavefunction of the atom at $\mathbf{R}_\alpha$. N denotes the number of unit cells. From the Bloch functions, an eigenfunction $\psi(\mathbf{k},\mathbf{r})$ of the sheet is expressed by

$$\psi(\mathbf{k},\mathbf{r}) = \sum_{j'=1}^{n} \mathcal{C}_{jj'}(\mathbf{k})\Phi(\mathbf{k},\mathbf{r}), \tag{2.4}$$

where $\mathcal{C}_{jj'}$ are the coefficients to be determined. Minimizing the energy functional

$$E_j(\mathbf{k}) = \frac{\langle\psi_j|\mathcal{H}|\psi_j\rangle}{\langle\psi_j|\psi_j\rangle}, \tag{2.5}$$

where $\mathcal{H}$ is the Hamiltonian of the graphene sheet, leads to the secular equation

$$\det[\mathcal{H} - E\mathcal{S}] = 0. \tag{2.6}$$

Here, $\mathcal{H}_{jj'}$ and $\mathcal{S}_{jj'}$ are called the transfer integral matrix and the overlap integral matrix, respectively:

$$\mathcal{H}_{jj'} = \langle\varphi_j|\mathcal{H}|\varphi_{j'}\rangle,\ \mathcal{S}_{jj'} = \langle\varphi_j|\varphi_{j'}\rangle,\ j, j' = 1...n. \tag{2.7}$$

For graphene, n=2. In the nearest-neighbor approximation, $\mathcal{H}$ and $\mathcal{S}$ are given by

$$\mathcal{H} = \begin{pmatrix} \epsilon_{2p} & tf(\mathbf{k}) \\ tf(\mathbf{k})^* & \epsilon_{2p} \end{pmatrix},\ \mathcal{S} = \begin{pmatrix} 1 & sf(\mathbf{k}) \\ sf(\mathbf{k})^* & 1 \end{pmatrix}, \tag{2.8}$$

where

$$f(\mathbf{k}) = e^{ik_x a/\sqrt{3}} + 2e^{-ik_x a/2\sqrt{3}}\cos(k_y a/2), \tag{2.9}$$

$$t = \langle\varphi_A(\mathbf{r} - \mathbf{R}_A|\mathcal{H}|\varphi_B(\mathbf{r} - \mathbf{R}_B)\rangle, \tag{2.10}$$

$$s = \langle\varphi_A(\mathbf{r} - \mathbf{R}_A|\varphi_B(\mathbf{r} - \mathbf{R}_B)\rangle. \tag{2.11}$$

s and t are called the transfer integral and the overlap integral between nearest neighbors A and B, respectively. Finally, the eigenvalues $E(\mathbf{k})$ are given by

$$E_{g2D}(\mathbf{k}) = \frac{\epsilon_{2p} \pm tw(\mathbf{k})}{1 \pm sw(\mathbf{k})}, \tag{2.12}$$

where $w(\mathbf{k}) = |f(\mathbf{k})|$. The positive/negative sign renders the bonding/antibonding π/π^*-band, respectively. For convenience, ϵ_{2p} is set to zero. If s is also set to zero, which is referred to as the Slater-Koster-scheme, the π- and π^*-bands become symmetric to each other with respect to $E = 0$. In this case, Eq.2.12 reads

$$E_{g2D}(k_x, k_y) = \pm t\left\{1 + 4\cos\left(\frac{\sqrt{3}k_x a}{2}\right)\cos\left(\frac{k_y a}{2}\right) + \cos^2\left(\frac{k_y a}{2}\right)\right\}^{1/2} \tag{2.13}$$

[10], where $t = -3.033$ eV is chosen in order to reproduce the first principles calculations for the graphite energy bands[11]. The bonding π-band is always energetically below the antibonding π^*-band, except at the degeneracy points (K-points), where the band splitting vanishes. Near the K-points, 2.13 is well approximated by

$$E(\mathbf{k}) = \pm\hbar v_{\mathrm{F}}|\mathbf{k} - \mathbf{k}_{K-\mathrm{point}}|, \tag{2.14}$$

with $v_{\mathrm{F}} \approx 0.8 \cdot 10^5$m/s, which is referred to as the "light cone approximation". The dispersion relation for graphene is depicted in Fig. 2.2

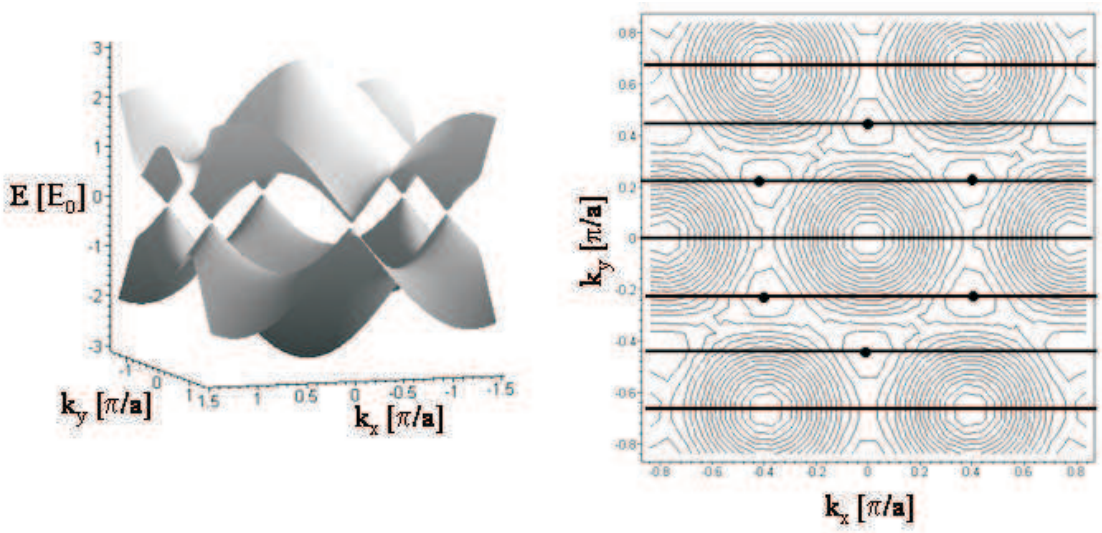

Figure 2.2: Left: Energy dispersion of the tight binding π- and π^*-band of graphene in units of E_0=3.033 eV. Right: Contour-plot of the bonding π-band. Lines denote the set of allowed k-vectors for a metallic (3,0) zigzag nanotube. Dots correspond to the K-points in the first Brillouin zone.

2.3 Zone Folding

From a graphene sheet, a nanotube is obtained by wrapping it into a seamless cylinder. Topologically, the wrapping is determined uniquely by the identification of two unit cells, which are connected by the so-called chiral vector

$$\mathbf{C}_\mathrm{h} \equiv (m, n) = m\mathbf{a}_1 + n\mathbf{a}_2, \tag{2.15}$$

with positive integers m and n. The nomenclature is "armchair tube" for m=n, "zigzag tube" for n=0, and "chiral tube" otherwise. The names reflect the shape of the cross-section of the tube, which is shown in Fig. 2.3.

The wrapping is equivalent to the imposing of periodic boundary conditions on the electronic wavefunction in the direction of $\mathbf{C}_\mathrm{h}$. This leads to a quantization of the electron wave vector $\mathbf{k}$ along the circumference of the tube:

$$\mathbf{k} \cdot \mathbf{C}_\mathrm{h} = 2\pi n, \tag{2.16}$$

where n is an integer. For the component of $\mathbf{k}$, which is parallel to the tube axis, continuous values $k_\parallel$ are allowed. This results in a backfolding of the graphene dispersion and thus the set-up of quasi-one dimensional subbands with index n. These 1D dispersion relations are given by substituting Eq. 2.16 into Eq.2.13. In reciprocal space, the set of allowed $\mathbf{k}$-vectors corresponds to parallel lines in the

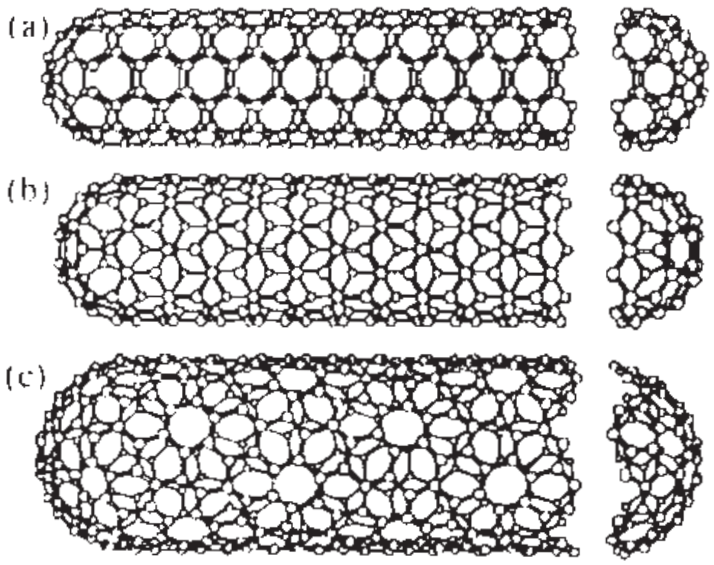

Figure 2.3: Classification of singlewall carbon nanotubes, corresponding to the shape of the π-bonds along the tube circumference. (A) An (m,m) armchair nanotube, (B) an (m,0) zigzag nanotube and (C) an (m,n) chiral nanotube. (Figure adapted from Ref. [9]

direction of the tube axis. In Fig. 2.2, the procedure is depicted for a (metallic) (3,0) zigzag nanotube. The 1D bands show a gap, if the K-points are not contained in the set of **k**-vectors. This is the case if $(2n + m)$ is a multiple of 3. Otherwise the tube behaves like a 1D metal, or, more exact, as a zero-gap semiconductor. For example, all armchair tubes are metallic, while one third of all zigzag tubes is metallic. In Fig. 2.4, the dispersion of the one-dimensional subbands with positive energy (with respect to the graphene Fermi level) are shown for a metallic (12,0) zigzag nanotube. The (π-orbital-)bands with negative energies are symmetric to the positive bands with respect to the graphene Fermi level. This energy level is referred to as the "charge neutrality point" in the following, since here the bands originating from the graphene π-band are completely filled, while the corresponding π^*-bands are empty.

2.4 Density of States

The one-dimensional dispersion relation allows to calculate the density of states (DoS). The result for a (12,0) nanotube is shown also in Fig. 2.4. The DoS shows

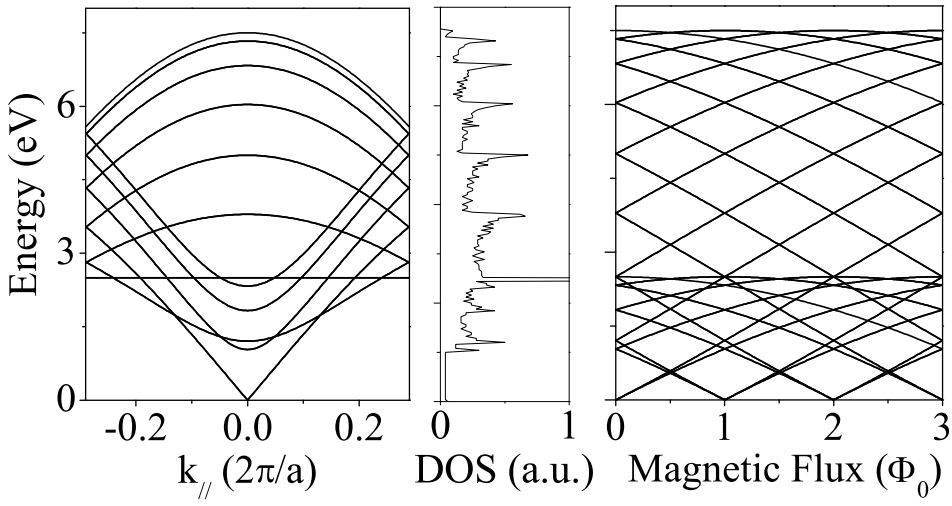

Figure 2.4: Left: Dispersion of the one-dimensional subbands of a (12,0) nanotube. Middle: Corresponding density of states. Right: Corresponding dispersion for $k_{\|}$=0 as a function of the magnetic flux through the tube cross section in units of $\Phi_0 = h/e$.

sharp van-Hove singularities, which are typical for one-dimensional systems. They arise at the energies of the onset of the (one-dimensional) subbands.
In the light-cone approximation (Eq. 2.14), the dispersion of the n-th one-dimensional subband for a tube with diameter d_{tube} is given by

$$E_n(k) = \pm E_0 \sqrt{\left(n - \frac{\beta}{3}\right)^2 + \left(\frac{k d_{\text{tube}}}{2}\right)^2}, \tag{2.17}$$

where $E_0 = (2\hbar v_{\text{F}})/(d_{\text{tube}})$ and β=0 for metallic and β=$\pm$1 for semiconducting tubes, respectively. k denotes the component of the **k**-vector in the direction of the tube axis. Each band contributes to the density of states ν via

$$\nu_n(E) = \frac{1}{\pi}\left(\frac{\mathrm{d}E_n}{\mathrm{d}k}\right)^{-1} = \frac{4}{\pi d_{\text{tube}} E_0} \frac{\frac{E}{E_0}}{\sqrt{\left(\frac{E}{E_0}\right)^2 - n^2}}, \tag{2.18}$$

giving rise to van-Hove singularities at the subband bottoms at $E = nE_0$. Thus, the subband spacing is given by E_0. For a given energy E, the number of electrons

$N_n(E)$ in the band n is obtained by integration,

$$N_n(E) = 4L \int_{nE_0}^{E} \nu_n(E')\mathrm{d}E' = 4\frac{2L}{\pi d_{\mathrm{tube}}}\sqrt{\frac{E}{E_0}^2 - n^2}, \tag{2.19}$$

where L is the length of the tube. Here, the prefactor 4 takes into account a fourfold band degeneracy, which originates from the spin degeneracy and from two K-points. The total number of electrons is then given by the sum over all bands between zero energy and the Fermi energy.
These approximations are valid in the limit of both large tube diameters and Fermi levels close to $E = 0$, since here only states near the K-points are occupied.

2.5 Magnetic Field

The tight-binding calculation for the electronic bandstructure of carbon nanotubes also allows for the inclusion of a static magnetic field. It has been shown that the Bloch functions in a static magnetic field can be expressed as

$$\Phi(\mathbf{k}, \mathbf{r}) = \frac{1}{\sqrt{N}} \sum_{\mathbf{R}} \exp(i\mathbf{k} \cdot \mathbf{R} + i\frac{e}{\hbar} G_{\mathbf{R}}) \varphi(\mathbf{r} - \mathbf{R}), \tag{2.20}$$

where $\mathbf{R}$ is a lattice vector and the phase factor $G_{\mathbf{R}}$ accounts for the Aharonov-Bohm phase of the electrons in the magnetic field [12]:

$$G_{\mathbf{R}}(\mathbf{r}) = \int_0^{\mathbf{R}} \mathbf{A}(\xi)\mathrm{d}\xi = \int_0^1 (\mathbf{r} - \mathbf{R}) \cdot \mathbf{A}(\mathbf{R} + \lambda[\mathbf{r} - \mathbf{R}])\mathrm{d}\lambda. \tag{2.21}$$

Here, $\mathbf{A}(\mathbf{r})$ is the vector potential associated to the magnetic field $\mathbf{B}$, $\mathbf{A} = \nabla \times \mathbf{B}$. The operation of the field dependent Hamiltonian

$$\mathcal{H} = \frac{1}{2m}(\mathbf{p} - e\mathbf{A})^2 + V \tag{2.22}$$

on the Bloch function 2.21 yields (finally)

$$\mathcal{H}\Phi(\mathbf{k}, \mathbf{r}) = \frac{1}{\sqrt{N}} \sum_{\mathbf{R}} \exp(i\mathbf{k} \cdot \mathbf{R} + i\frac{e}{\hbar} G_{\mathbf{R}}) \left[\frac{\mathbf{p}^2}{2m} + V\right] \varphi(\mathbf{r} - \mathbf{R}). \tag{2.23}$$

This means that the Hamiltonian matrix element in a magnetic field is obtained by multiplying the corresponding matrix element in zero field by a phase factor.

2.5.1 Parallel Field: Aharonov-Bohm effect

For a magnetic field pointing in the direction of the tube axis, the tight-binding calculation gives a transparent result. An electron can gain an Aharonov-Bohm phase only by propagation around the tube. Thus, the wave vector component $k_\parallel$ parallel to the tube axis remains unchanged, while the quantization condition for the transverse component $k_\perp$ becomes magnetic-field dependent:

$$k_\parallel \longrightarrow k_\parallel, \tag{2.24}$$

$$k_\perp \longrightarrow k_\perp + \frac{\Phi}{L\Phi_0}, \tag{2.25}$$

where Φ is the magnetic flux, $\Phi_0 = h/e$ is the flux quantum and L is the nanotube circumference.
This leads to the important result that for both metallic and semiconducting tubes, a gap opens and closes as a function of magnetic flux through the tube with a period of Φ_0. The position of the subband onsets as a function of the magnetic field is depicted in Fig. 2.4. At zero energy, a gap opens and closes periodically. Hence, a parallel magnetic field is predicted to periodically turn a metallic tube into a semiconducting one and back.

2.5.2 Perpendicular Field: Quantum Oscillations

If the magnetic field is perpendicular to the tube axis, the tight binding calculation is no more straight-forward. In the limit of large fields, where the magnetic length

$$\ell_\mathrm{m} = \sqrt{\frac{\hbar}{eB}} \tag{2.26}$$

becomes much smaller than the tube diameter, the tight binding calculation predicts a decreasing dispersion of the subbands n, i.e. $\mathrm{d}E_n/\mathrm{d}k$ is decreasing for all values of k. The positions of the bands are predicted to oscillate as the field is increased. The amplitude of the oscillations is getting smaller, but never vanishes completely (see [9]). This results in a considerable variation of the density of states as a function of the magnetic field.
In the framework of $\mathbf{k}\cdot\mathbf{p}$-perturbation theory, the formation of Landau levels with a vanishing dispersion is predicted. The energy of the Landau levels is predicted to converge to the energies of the graphene Landau levels [13].

Chapter 3

Transport Properties of Carbon Nanotubes

In this section a few effects concerning electronic transport in mesoscopic systems are described. Since in carbon nanotubes a huge amount of such effects seem to be present, a comprehensive review is beyond the scope of this thesis. Therefore only those have been selected, which are substantially necessary to understand the results of the measurements, which are presented in the subsequent sections.

3.1 Quantum Interference

In diffusive mesoscopic samples, where electronic transport is coherent, quantum interference effects contribute significantly to the conductance. We report briefly the conductance changes introduced by the closely related phenomena of weak localization, the Aharonov-Bohm effect and universal conductance fluctuations. The following subsections are adapted mainly from the article by Beenakker and van Houten [14].

3.1.1 Weak localization

Being developed in 1979 by Anderson *et al.* [15] and Gorkov *et al.* [16], the theory of weak localization gives an explanation for the negative magnetoresistance of disordered conductors. In addition, it represents an elegant and direct measure of the phase coherence length of the electrons. The latter is defined as the length on which the electron can interfere with itself or, in other words, the length on which

the electron motion can be described by a single particle Schrödinger equation.
In the Feynman path description [17] of diffusive transport, the basic idea of weak localization is given as follows: The probability $P(\mathbf{r}, \mathbf{r}', t)$ for motion from point $\mathbf{r}$ to $\mathbf{r}$' during the time t is given by

$$P(\mathbf{r}, \mathbf{r}', t) = \left| \sum_i A_i \right|^2 = \sum_i |A_i|^2 + \sum_{i \neq j} A_i A_j^* \ , \tag{3.1}$$

where A_i are the probabilities for each single trajectory i connecting $\mathbf{r}$ and $\mathbf{r}$'. Assuming that the Fermi wavelength is small compared to the separation between the scattering events, the sum can be restricted to classical paths. If $\mathbf{r} \neq \mathbf{r}'$, the right hand term in 3.1 averages out and $P(\mathbf{r}, \mathbf{r}', t)$ equals the classical value. If beginning and end point coincide, the contributions to the sum in 3.1 can be grouped in time-reversed pairs A^+ and A^-. Time reversal implies that the amplitudes of the two paths are identical, $A^+ = A^- = A$. Therefore, the probability of coherent backscattering

$$P(\mathbf{r}, \mathbf{r}, t) = \left| A^+ + A^- \right|^2 = 4 \left| A \right|^2 \tag{3.2}$$

is twice the classical value, which reduces the diffusion constant and hence the conductivity. This is the basic principle of weak localization.
The number of paths participating in coherent backscattering is limited by the phase coherence length $L_\varphi = \sqrt{D\tau_\varphi}$, where D is the diffusion constant and τ_φ is the phase coherence time. For a rectangular conductor of width W one speaks of 2D or 1D weak localization if $L_\varphi > W$ or $L_\varphi < W$. For this work, only 1D weak localization will be of interest. The conductance change ΔG_{WL} due to weak localization is given by $\Delta G_{\mathrm{WL}} = (e^2/h)(L_\varphi/L)$ [18], where L is the length of the conductor.
Application of a magnetic field perpendicular to the closed electron orbits breaks the time reversal invariance and hence reduces the enhanced backscattering. In their way around the loop the electrons gain the Aharonov Bohm phase

$$\Phi_{\mathrm{AB}} = \frac{1}{\hbar} \oint \mathbf{p} \cdot d\mathbf{l} \ , \tag{3.3}$$

where $\mathbf{p} = m\mathbf{v} - e\mathbf{A}$ is the canonical momentum and $\mathbf{A}$ is the vector potential of the magnetic field. For a pair of time reversed loops this leads to a phase difference

$$\Delta\Phi_{\mathrm{AB}} = \frac{1}{\hbar} \oint_+ \mathbf{p}^+ \cdot d\mathbf{l} - \frac{1}{\hbar} \oint_- \mathbf{p}^- \cdot d\mathbf{l} \tag{3.4}$$

$$= \frac{2e}{\hbar} \int (\nabla \times \mathbf{A}) \cdot d\mathbf{S} = \frac{2eBS}{\hbar} = \frac{2S}{L_{\mathrm{m}}^2} = 4\pi \frac{\Phi}{\Phi_0} \tag{3.5}$$

where S is the loop area, $L_{\mathrm{m}} = (\hbar/eB)^{1/2}$ is the magnetic length, Φ is the magnetic flux and $\Phi_0 = h/e$ is the flux quantum for normal conductors. In a magnetic field, loops enclosing areas $S > L_{\mathrm{m}}^2$ do no longer contribute, since on average

the counterpropagating loop does not interfere constructively. Therefore the magnetic length enters into the full expression for the 1D weak localization correction ($L_\varphi, L_\mathrm{m} \gg W \gg L_\mathrm{el}$)

$$\Delta G_\mathrm{WL}^\mathrm{1D} = -\frac{e^2}{\pi\hbar}\frac{1}{L}\left[\frac{3}{2}\left(\frac{1}{D\tau_\varphi}+\frac{4}{3D\tau_\mathrm{SO}}+\frac{1}{D\tau_\mathrm{B}}\right)^{-1/2}-\frac{1}{2}\left(\frac{1}{D\tau_\varphi}+\frac{1}{D\tau_\mathrm{B}}\right)^{-1/2}\right], \tag{3.6}$$

where $\tau_\mathrm{B} = (3L_\mathrm{m}^4)/(W^2D)$, τ_SO is the spin-orbit scattering time and D is the diffusion constant [18]. Note that the theory of weak localization was developed for planar metal films. In the case of a (cylindrical) nanotube in a magnetic field perpendicular to the tube axis, this expression is, strictly speaking, not correct. Since no theory of weak localization for this geometry exists, the above expression is used as an approximation, which turns out to work rather good.

3.1.2 Aharonov-Bohm effect

If we consider a ring-shaped conductor, only Feynman paths along the two arms of the ring are allowed. Assume that the magnetic flux through the ring is changed by $\Delta\Phi = S \cdot \Delta B = h/e$, where S is the area enclosed by the ring. Thereby the phase difference between the two paths changes by 2π. This means that the conductance of the ring is periodically modulated by Φ with a period h/e:

$$G(\Phi) = G\left(\Phi + n\left(\frac{h}{e}\right)\right), \tag{3.7}$$

which is referred to as the h/e Aharonov-Bohm effect [8]. The second harmonic with a period of $\Delta\Phi = h/2e$ is caused by the interference between trajectories which interfere after one revolution around the ring. This oscillation contains a contribution from time-reversed trajectories which also cause the weak localization effect. Hence, the $h/2e$-oscillation can be seen as a periodic modulation of the weak localization effect.

An important point is that, the coherent backscattering by pairs of time-reversed trajectories, the $h/2e$ oscillation results always in a conductance minimum at $B = 0$ and thus a sample independent phase. This must be contrasted with the h/e-oscillations, whose phase varies randomly for different impurity configurations. For cylinder-shaped conductors, which can be regarded as many rings in parallel, the h/e-oscillations are thus predicted to average out, while the $h/2e$-oscillations remain. An exact theoretical treatment of the $h/2e$-oscillations in cylinders was performed by Altshuler, Aronov and Spivak in 1981 [19]. The calculation also takes into account a non-vanishing magnetic flux inside the cylinder walls, which corresponds to a finite

wall thickness. The result for the conductance change $\Delta G_1(B)$ is

$$\Delta G(B) = -\frac{e^2}{\pi^2\hbar}\frac{2\pi R}{L}\left[\ln\frac{L_\varphi(B)}{L_{\rm el}} + 2\sum_{n=1}^{\infty} K_0\left(n\frac{2\pi R}{L_\varphi(B)}\right) \times \cos\left(2\pi n\frac{2\Phi}{\Phi_0}\right)\right], \quad (3.8)$$

where K_0 is the McDonald function and

$$\frac{1}{L_\varphi^2(B)} = \frac{1}{L_\varphi^2} + \frac{1}{3}\left(\frac{2\pi aB}{\Phi_0}\right)^2, \quad (3.9)$$

where a is the cylinder wall thickness. If the cylinder is tilted by a small angle Θ with respect to the magnetic field, a is rescaled to an effective wall thickness a^* by

$$a^* = \sqrt{a^2\cos^2\Theta + 6R^2\sin^2\Theta}\ . \quad (3.10)$$

For $a > 0$, Eq. 3.8 predicts that the oscillation amplitude of $\Delta G_(B)$ decreases with increasing magnetic field. In addition, a monotonic component appears in the magnetic field dependence of the conductance, which originates from conjugated paths which do not enclose the cylinder axis. For phase coherence lengths smaller than the cylinder circumference, the amplitude of the oscillations is exponentially damped.

3.1.3 Universal Conductance Fluctuations

In a classical diffusive conductor, sample-to-sample fluctuations in the conductance can be neglected. If one assumes a narrow wire of length L, which consists of independently fluctuating segments of the elastic mean free path L_{el}, then the root mean square (rms) δG of the conductance fluctuations is given by $\langle G\rangle \times (L_{el}/L)^{1/2}$. Therefore, the fluctuations are suppressed with an increasing number of segments. Quantum interference on the other hand leads to significant sample-to-sample fluctuations, if the sample size is of the order of the phase coherence length L_φ. Then the conductance depends crucially on the exact impurity configuration. Altshuler, Lee and Stone derived that for a phase coherent conductor of length L and width W the rms conductance fluctuations are given by

$$\delta G = 0.73\left(\frac{2e^2}{h}\right), \quad (3.11)$$

if $L_\varphi > W, L$ and $L \gg W$ [20, 21] . The magnitude of the fluctuations is independent of both the sample size and the degree of disorder. Hence they are referred to as "universal conductance fluctuations".

In the experimental situation conductance fluctuations can also be induced by changing the Fermi energy E_F or the magnetic field B. In order to achieve an equivalent to the complete change of the impurity configuration, the change in E_F and B must be larger than the correlation energy ΔE_F or the correlation field ΔB. Note that the correlation field/energy must be small enough not to change the statistical properties of the ensemble.
At nonzero temperatures, the amplitude of the fluctuations is reduced for two reasons. On one hand, the phase coherence length becomes shorter with increasing temperature. On the other hand, thermal averaging occurs, which is expressed by the thermal length $L_T = (\hbar D/k_B T)^{1/2}$. An exact calculation gives the magnitude of the fluctuations at finite temperatures for two different regimes. If $L_\varphi \ll L, L_T$, the thermal length does not enter and

$$\delta G_\mathrm{rms} = \sqrt{12}\frac{2e^2}{\hbar}\left(\frac{L_\varphi}{L}\right)^{3/2}. \tag{3.12}$$

If $L_T \ll L_\varphi \ll L$, then

$$\delta G_\mathrm{rms} = \left(\frac{8\pi}{3}\right)^{1/2}\frac{2e^2}{\hbar}\frac{L_T L_\varphi^{1/2}}{L^{3/2}} \tag{3.13}$$

[22, 23] . Note that L_φ enters these relations with a different exponent. Hence, from the experimental results for L_φ one can decide which transport regime is actually present in the sample.

3.2 Coulomb Interaction

The electron-interference mechanisms described in the preceding sections only account for single particle effects. If Coulomb interaction between electrons is considered, additional transport features arise. Three, conceptually different approaches are mentioned here: Nyquist dephasing describes the phase breaking due to weak electron-electron interactions in a perturbative way. Zero bias anomalies of the conductance occur at tunneling into a gas of interacting electrons, while the Coulomb blockade describes the interaction via the electrostatic energy of an additional charge on a small conducting island. The introduction into Coulomb blockade follows the lines of L. Kouwenhoven [24] and H. Grabert *et al.* [25].

3.2.1 Nyquist Dephasing

If one has measured the phase coherence length, the question arises, which phase breaking mechanism dominates. In carbon nanotubes, possible candidates are the

electron-phonon scattering, scattering from magnetic impurities, which are left from the nanotube growth process, and electron-electron scattering. The latter has turned out to be the most appropriate mechanism for diffusive metal films and also for nanotubes at low temperatures. Thus, we will summarize the corresponding theoretical predictions as given by Altshuler, Aronov and Khmelnitskii [26].
The calculation first takes into account the action of an external high frequency electric field on quantum corrections to conductivity. The result is then generalized to thermal electromagnetic fluctuations of the electron gas.
Consider a closed electron path and let the motion start at time $-t$ and be accomplished at t. An alternating electric field $E(t)$ induces a phase difference $\Delta\varphi$ between the clockwise and counterclockwise propagating path, which equals

$$\Delta\varphi = \frac{e}{\hbar}\int_{-t}^{t} \mathrm{d}\tau \int_{-\tau}^{\tau} \mathrm{d}\tau' \left[\mathbf{E}(\tau')\mathbf{v}(\tau') - \mathbf{E}(\tau')\mathbf{v}(-\tau')\right] \ , \tag{3.14}$$

where $\mathbf{v}(\tau)$ is the electron velocity at time τ.
Application of diagrammatic perturbation theory on the electron motion in the electric field fluctuations of the sample yields a characteristic phase breaking time τ_φ of the order of

$$\tau_\varphi \sim \left(\frac{\hbar^2 D^{1/2}\nu a^2}{T}\right)^{2/3} \ , \tag{3.15}$$

and a characteristic length

$$L_\varphi = \sqrt{D\tau_\varphi} \sim \left(\frac{\hbar^2 D^2 \nu a^2}{T}\right)^{1/3} \ , \tag{3.16}$$

where D is the diffusion constant and ν is the density of states at the Fermi level. The result is valid if $a \ll L_\varphi$, where a is both the sample width and height (1D case). Introducing the conductance $\sigma = e^2 D\nu a^2$ yields, finally

$$L_\varphi \sim \left(\frac{\hbar^2 D\sigma}{e^2 T}\right)^{1/3} \ . \tag{3.17}$$

Note that T enters with a characteristic exponent of $-1/3$, which is a hallmark of electron-electron scattering as the dominating dephasing mechanism in the experiment.

3.2.2 Zero Bias Anomalies

In single wall carbon nanotubes, the electron transport is predicted to be one-dimensional and ballistic, even in the presence of weak disorder [27, 28], which

gives rise to a strong effect of electron-electron interactions, resulting in the establishment of a Luttinger liquid. A Luttinger liquid is predicted to emerge in 1D systems, where Coulomb interaction between the electrons leads to the breakdown of the Fermi liquid state. The excitations of the system are rather of bosonic nature (charge/spin-density waves) with a linear dispersion relation. This leads to a power law behavior of the system's tunneling density of states (TDOS),

$$\nu(E) \propto E^{\alpha} \ , \tag{3.18}$$

with a positive exponent α, which reflects the interaction strength as well as the tunneling geometry [29]. For metallic tunneling contacts, one also obtains power laws for the tunneling conductance from the TDOS:

$$G(T) \propto T^{\alpha} \ , \tag{3.19}$$

$$G(V) \propto V^{\alpha} \ , \tag{3.20}$$

where T is the temperature and V is the bias voltage of the tunnel junction. Zero bias anomalies are typical for Luttinger liquid behavior have been indeed been observed for singlewall nanotubes [30].
The subband spacing of multiwall tubes is by a factor of the order 10 smaller than that of singlewall tubes, and a strong doping is reported [31]. Hence, transport is likely to occur through more than one channel and the 1D LL picture is probably not applicable. Both the nature of the excitations and the power law scaling are reproduced also by the unconventional Coulomb blockade theory [32], which describes an interacting, disordered conductor coupled to high-impedance transmission lines by a single tunnel junction. Here the quasiparticle tunneling into the conductor is suppressed at bias voltages $V < e/2C$, where C is the total capacitance of the conductor, and charge is transferred by 1D plasmon modes. A zero-bias anomaly similar to that in Luttinger liquids is also predicted with an exponent

$$\alpha = \left(\frac{R}{hD\nu_0}\right) \log(1 + \nu_0 U_0) \ , \tag{3.21}$$

where D is the diffusion constant, $\nu_0 = M/(h v_{\mathrm{F}})$ is the noninteracting density of states, and M is the number of transport channels. U_0 is an effective short 1D interaction and R denotes the tube radius. For weak interactions, the logarithmic term is of order unity and with $D \approx v_{\mathrm{F}} L_{\mathrm{el}}$ one obtains

$$\alpha \approx \frac{R}{M L_{\mathrm{el}}} \tag{3.22}$$

and α represents a measure of the elastic mean free path L_{el}.
This model seems more appropriate for (multichannel) multiwall tubes, since it

additionally predicts a transition from a power law to Ohmic behavior at high bias voltages. This has been observed experimentally [33]. In addition, Kanda *et al.* reported a strong variation of the tunneling exponent with Fermi energy [34], which also favors Coulomb blockade beyond the orthodox theory.

3.2.3 Coulomb Blockade

For a carbon nanotube, which is only weakly coupled to the leads, static Coulomb interactions may affect the electronic transport properties. The energy scale for adding an extra electron to the tube is given by

$$E_{\mathrm{Ch}} = \frac{e^2}{2C_\Sigma} \ , \tag{3.23}$$

where C_Σ is the total capacitance of the system. Coulomb blockade arises if E_{Ch} exceeds the thermal energy $k_{\mathrm{B}}T$.
A nanotube with weak coupling to the leads can be modeled by a single electron transistor (SET). A SET consists of a metallic island with two tunnel contacts (L/R) and a gate electrode (See Fig. 3.1). Neglecting the discrete levels in the tube, the

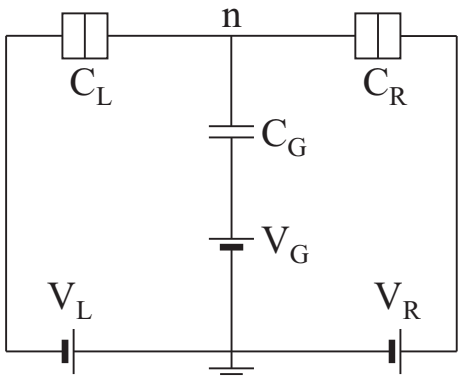

Figure 3.1: Single electron transistor. A metallic island containing n excess electrons is coupled to source/drain voltages $V_{\mathrm{L/R}}$ via tunnel junctions with capacitances $C_{\mathrm{L/R}}$. A gate voltage V_{G} is applied by a capacitor C_{G}.

charging energy is given by

$$E_{\mathrm{Ch}} = \frac{(ne - Q_{\mathrm{G}})^2}{2C_\Sigma}, \tag{3.24}$$

where $C_\Sigma = C_{\mathrm{L}} + C_{\mathrm{R}} + C_{\mathrm{G}}$ is the total capacitance of the tube, consisting of the capacitances $C_{\mathrm{L/R}}$ of the left and right tunnel junction and the gate capacitance C_{G} [24]. In the case of a quantum dot with discrete electron levels, this is modified to

$$E_{\mathrm{Ch}}^{\mathrm{Dot}} = E_{\mathrm{Ch}} + \delta E, \tag{3.25}$$

where δE is the level spacing. Accounting for spin, one level can accomodate two electrons and hence δE equals zero for the second electron in the level. For carbon nanotubes one expects even four lectrons per level, due to spin- and band-degeneracy (see Chap. 2).
If an additional electron $(n+1)$ tunnels into the tube, E_{Ch} changes by

$$\Delta E_{\mathrm{Ch}}(n+1, Q_{\mathrm{G}}) = E_{\mathrm{Ch}}(n+1, Q_{\mathrm{G}}) - E_{\mathrm{Ch}}(n, Q_{\mathrm{G}}) = \left(n + \frac{1}{2} - \frac{Q_{\mathrm{G}}}{e}\right) \frac{e^2}{C_{\Sigma}}. \quad (3.26)$$

The energy differences are equally spaced and are tuned by the gate voltage, as depicted in Fig. 3.2. An electron can enter/leave the tube if the chemical potential

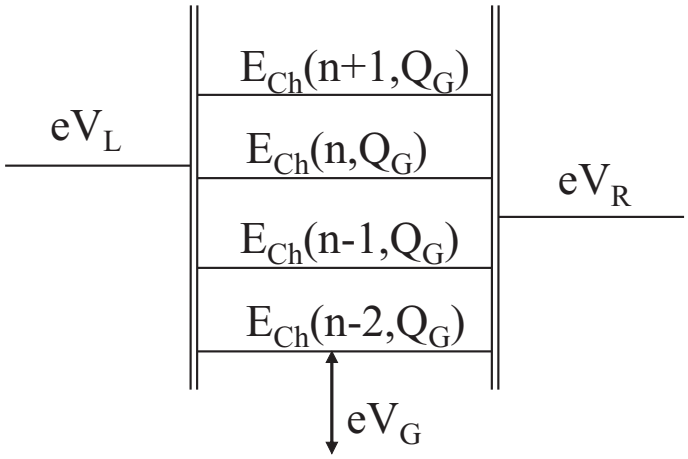

Figure 3.2: Addition energies $\Delta E_{\mathrm{Ch}}(n, Q_{\mathrm{G}})$ for n excess electrons on an island, which is coupled by tunneling barriers to metallic leads with chemical potentials $eV_{\mathrm{L/R}}$. V_{G} is the gate voltage.

$\mu_{\mathrm{L/R}}$ of the left/right lead is larger/smaller than $\Delta E_{\mathrm{Ch}}(n+1, Q_{\mathrm{G}})$. Hence current can flow through the transistor only if

$$eV_{\mathrm{L}} > \Delta E_{\mathrm{Ch}}(n+1, Q_{\mathrm{G}}) > eV_{\mathrm{R}} \quad (3.27)$$

is satisfied. Thus, by variation of the gate voltage U_{G}, periodic current oscillations are produced (Coulomb oscillations). Alternatively, transport can be established by applying a sufficient bias voltage difference $V_{\mathrm{Bias}} = V_{\mathrm{L}} - V_{\mathrm{R}}$. Otherwise, the current flow will be suppressed (Coulomb blockade). Quantitatively, the regions in the $(U_{\mathrm{G}}, V_{\mathrm{Bias}})$-plane, where current is suppressed, have a diamond-like shape (Coulomb diamonds), whose edges are given by the conditions

$$e(n - \frac{1}{2}) < C_{\mathrm{G}}U_{\mathrm{G}} + (C_{\mathrm{L}} + \frac{1}{2}C_{\mathrm{G}})V_{\mathrm{Bias}} < e(n - \frac{1}{2}) \quad (3.28)$$

$$e(n - \frac{1}{2}) < C_{\mathrm{G}}U_{\mathrm{G}} - (C_{\mathrm{R}} + \frac{1}{2}C_{\mathrm{G}})V_{\mathrm{Bias}} < e(n - \frac{1}{2}) \quad (3.29)$$

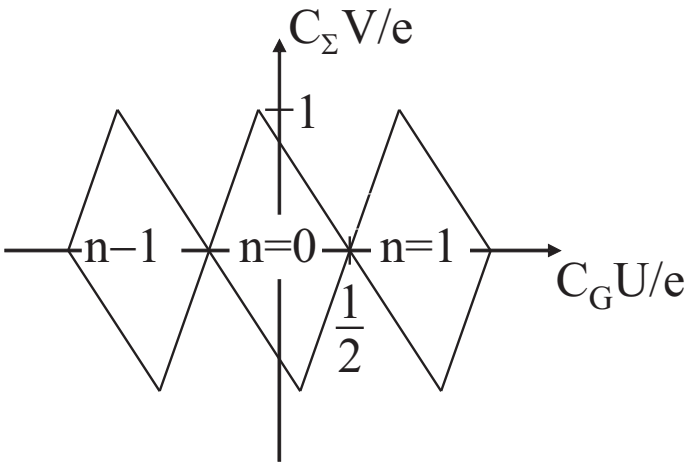

Figure 3.3: Coulomb diamonds: regions of current suppression of a SET in the (U_{gate},V_{bias})-plane for n excess electrons on the island. C_Σ and C_G are the gate capacitance and the total capacitance, respectively.

[25]. This is also shown in Fig. 3.3. From 3.28 and 3.29 we derive that the gate capacitance C_{G} is given by $C_{\text{G}} = e/U_{\text{D}}$, where U_{D} is the width of the Coulomb diamonds, while the total capacitance is given by their height V_{D} by $C_\Sigma = e/V_{\text{D}}$. From the slope of the edges, the junction capacitances can also be extracted. Hence, Coulomb blockade is an effective tool to investigate the electrostatic quantities of a given sample.

Chapter 4

Sample Preparation and Measurement Setup

4.1 Nanotube Material

All nanotubes used in this work are multiwall carbon nanotubes (MWNTs), which consist of several concentric singlewall shells. The MWNT diameters range from 3 nm to 50 nm, while the lengths are a few 100 nm up to 10 μm.
The tubes were grown by arc-discharge [2]. This method has the advantage that no ferromagnetic catalyst particles are required, which could contaminate the tubes with magnetic impurities. The material was produced by the group of L. Forró at the EPFL (Lausanne). After the growth, the material was purified for a large nanotube yield, with respect to the remaining amorphous carbon particles [35].

4.2 Device Fabrication by Random Dispersion

The devices required for this work consisted of a single MWNT with ohmic contacts and a gate electrode. The basic design of the samples is mainly inspired by Refs. [36, 37].
As a starting point, an oxidized Si wafer with an oxide thickness of 600 nm was coated with Cr/Au alignment marks. Afterwards, Al strips of width 10 μm, length 100 μm, thickness 40 nm and bonding pads were evaporated on the chip. By exposure to air, these strips have been covered by an electrically insulating, native oxide layer (Al_2O_3). Thus, the Al strips served as gate electrodes for the MWNTs, which were deposited in the next step. Therefore, the tubes had been dispersed in

chloroform by the aid of supersonic vibration. The suspension was brought on the chip and removed immediately by nitrogen flow. As a result, individual MWNTs are deposited randomly on the chip. Afterwards the chip was cleaned in propanol, in order to remove unwanted deposits like amorphous carbon.
Next, isolated MWNTs were detected in a scanning electron microscope and the tube's coordinates with respect to the alignment marks were notified. Subsequently, the chip was spin-coated with a layer of PMMA (polymethylmethacrylate), in which the structure of the source and drain contacts was patterned by electron beam lithography. The exposed PMMA was then removed by a mixture of MIBK (methylisobutylketone) and propanol (1:3) and rinsing in pure propanol. In order to remove the residual developed resist, a short (3 s) oxygen plasma treatment was performed. Then, 80 nm of Au were evaporated thermally in vacuum ($\approx 10^{-6}$ mbar) and a lift-off was done in acetone. The chip was then glued into a commercially available chip-carier and wired by ultrasonic bonding. A typical sample obtained this way is shown in Fig. 4.1.

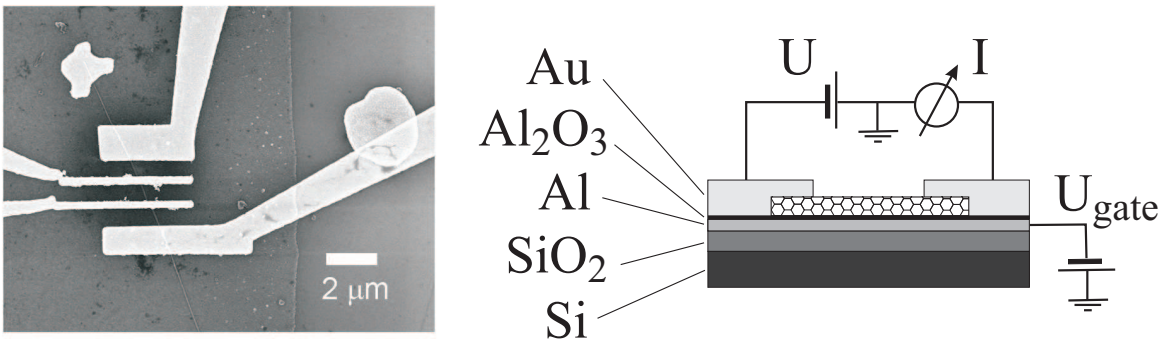

Figure 4.1: Left: Scanning-electron microscopy image of a sample as produced by random nanotube dispersion. Single multiwall carbon nanotubes were deposited on an Al strip and contacted with 300 nm spaced Au fingers from above. The Al strip under the tube serves as a backgate. Right: Schematic view of the sample. A constant bias voltage U is applied and the current I is measured. A gate voltage U_{gate} is applied to the Al backgate.

4.3 Device Fabrication by Electrostatic Trapping

For a controlled placement of MWNTs on top of a gate electrode, an ac electric field was used. The procedure performed in this work is similar to that of Krupke [38], and uses the fact that a nanotube is dragged into the direction of the gradient of an external electric field by the induced (electric) dipole momentum.

For our samples, a narrow Al strip of width $\sim 2\mu$m was produced, which is located between two fan-shaped Al electrodes. The fan-shaped electrodes were used to create a strong "trapping"-field in order to align nanotubes between them. The medium strip serves as a backgate, similar to the Al backgate in the preceding section. At this stage, the chip was bonded into a chip carrier and connected in series with a 350 MΩ resistor. MWNTs were suspended in propanol, and a droplet of the suspension was put on the chip. A voltage of $V_{\mathrm{rms}} = 10$ V at a frequency of 3 MHz was applied to the fan-shaped electrodes for 3 min. Afterwards, the suspension was removed and the voltage was turned off. As a result, nanotubes are trapped between the electrodes and spanned across the gate. The suspension was then removed from the chip carrier and the nanotube was equipped with Au contacts as described above.
The trapping appears to be self-stopping, i.e. usually only one tube at maximum is trapped at one pair of electrodes. We assume that the tube causes a capacitative shortcut, which leads to the breakdown of the trapping field and thus prevents other tubes from attaching. Note that no current can flow through the tube, since the electrodes are covered with insulating Al_2O_3 native oxide. A typical sample as processed this way is presented in Fig. 4.2.

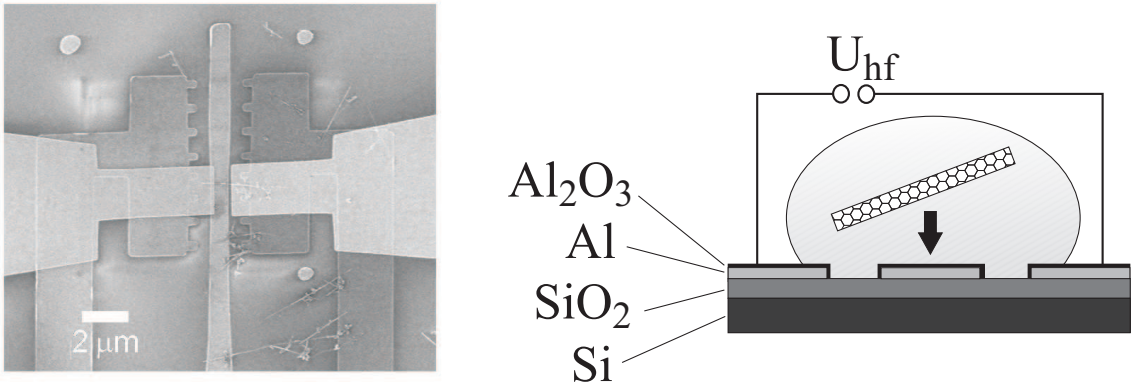

Figure 4.2: Left: Scanning-electron microscopy image of a sample as produced by nanotube trapping. A single multiwall carbon nanotube is trapped between two Al electrodes and contacted with 600 nm spaced Au fingers from above. The Al finger under the tube serves as a backgate. Right: Sketched trapping procedure. A high frequency voltage U_{hf} is applied to the fan-shaped trapping electrodes, which spans a nanotube across the central Al gate electrode.

4.4 Measurement Circuitry and Cryostats

The electronic transport measurements on multiwall carbon nanotubes, as described in this work, were carried out in two dilution refrigerators. The dilution systems were a toploading refrigerator from Oxford Cryogenics with a base temperature of 25 mK and a conventional refrigerator from Air Liquide, base temperature 20 mK. Both systems were equipped with radio-frequency (RF) filters at room temperature (π-filters). In order to keep the electron temperature close to the bath temperature, the Air Liquide system was equipped additionally with two stages of copper powder RF filters. The first stage was located at the still level (T$\sim$1K), while the second one was mounted directly above the sample holder at base temperature. These filters provided a cutoff frequency of $f \approx 300$ MHz. This was sufficient to shield the 4.2 K blackbody radiation of the helium bath, since $f_{\max}(4.2\mathrm{K}) = 2.82 \cdot (4.2\mathrm{K}) \cdot k_\mathrm{B}/h \approx$ 245 GHz according to Wien's law. The conductance of the nanotube was measured

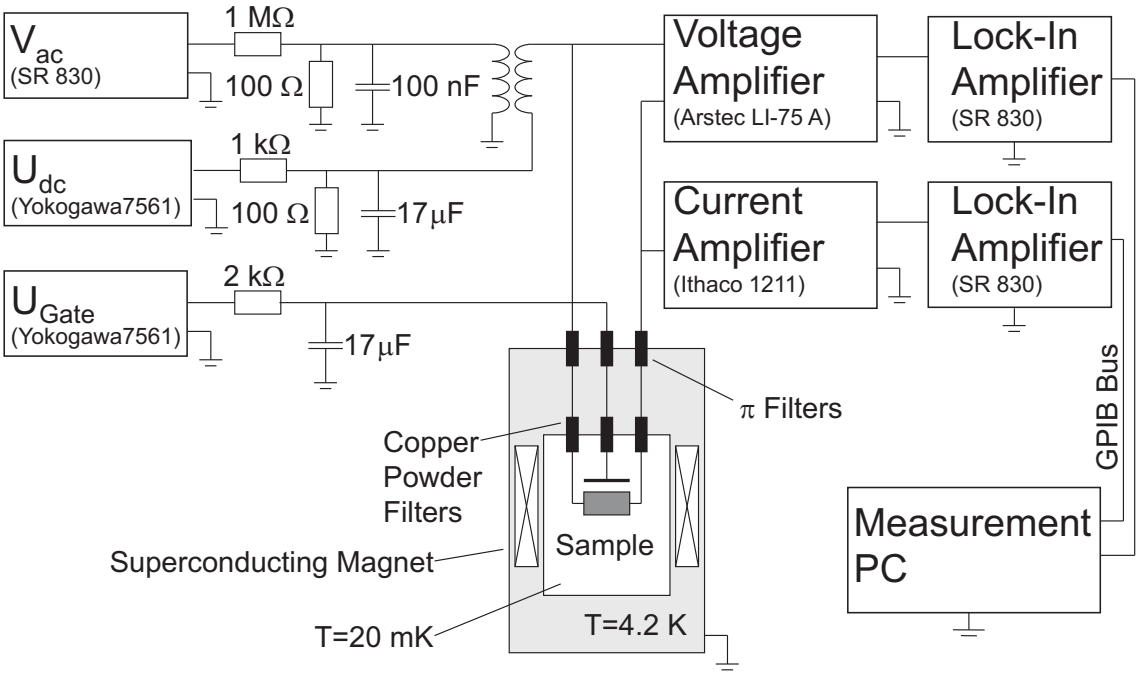

Figure 4.3: Measurement circuitry as used with the Air-Liquide refrigerator. Voltage dividers and low-pass filters, as well as current and voltage pre-amplifiers are used for noise reduction.

in a two-point geometry with a lock-in technique: a constant low bias ac voltage V_{ac} was applied and the current through the sample was converted to a voltage by a current amplifier (Ithaco 1211 Current Amplifier), which in turn was read out by a lock-in amplifier (EG&G 7265 for the Oxford system, Stanford Research 830 for

the Air Liquide refrigerator).
Additionally, a dc bias voltage V_{dc} was applied by a Yokogawa 7651 voltage source. An identical device was used to apply a gate voltage U_{gate}. A detailled diagram of the circuitry is presented in Fig. 4.3. Note that all voltage sources have been equipped with voltage dividers and low-pass filters for noise reduction.
The construction of the sample holders including the wiring and RF filtering was also done within this thesis. The sample holder for the Air Liquide system was built up in collaboration with J. Bentner.
Magnetic fields are applied with superconducting magnets and Oxford IPS 120 power supplies. The maximum fields available were 8 T (Air Liquide) and 19 T (Oxford). In addition, for the Oxford system a rotatable sample holder has been used, which allows in-situ change of the angle of the magnetic field with respect to the tube axis.
The collection of the large amount of data in this thesis required the development of a fast data-acquisition scheme. Eventually, it turned out that slow charge relaxation processes, most probably in the oxide layer, limited the speed of the data acquisition to 5 samples/sec. At higher rates, the sweeps of the gate voltage U_{gate} resulted in a poor reproducibility of the G vs. U_{gate}-traces.

Chapter 5

Motivation and Preliminary Measurements

In this section, motivations for the measurements done within this work are given. One of them is the lack of comprehensive transport studies on multiwall carbon nanotubes in literature. In addition, the results of preliminary measurements indicate the direction for the focus of the main investigations in this thesis.
Apart from this work, the present section has been published in *New Journal of Physics* [39].

5.1 Motivation

Quantum transport in multiwall carbon nanotubes has been intensely studied in recent years [3, 40]. Despite some indications of ballistic transport even at room temperature [41, 42], the majority of experiments revealed typical signatures of diffusive quantum transport in a magnetic field B such as weak localization (WL), universal conductance fluctuations (UCF) and the $h/2e$-periodic Altshuler-Aronov-Spivak (AAS) oscillations [3, 43, 44, 45]. These phenomena are caused by the Aharonov-Bohm phase, either by coherent backscattering of pairs of time-reversed diffusion paths (WL and AAS) or by interference of different paths (UCF), see Chap. 3. In addition, zero bias anomalies caused by electron-electron interactions in the differential conductance have been observed [46]. In those experiments, the multiwall tubes seemed to behave as ordinary metallic quantum wires. On the other hand, bandstructure calculations for singlewall and doublewall nanotubes predict strictly one-dimensional transport channels, which give rise to van Hove singularities in the density of states (see Chap. 2), even if inter-wall couping is taken into account [47].

Experimental evidence for this has been obtained mainly by electron tunneling spectroscopy on single wall nanotubes [48]. In this picture of strictly one-dimensional transport, a quasiclassical trajectory cannot enclose magnetic flux and no low-field magnetoconductance is expected. Hence, the question arises how the specific band structure is reflected in the conductance as well as in its quantum corrections and how those on first glance contradictory approaches can be merged into a consistent picture of electronic transport.
From the experimental point of view, addressing these problems is only possible, as soon as the electronic Fermi level can be shifted over a considerably large energy range. This allows for studying the electronic transport properties in the vicinity of the charge neutrality point, where bands with negative energy are completely occupied, whereas those with positive energies are completely empty. This regime could not be accessed in most of the electronic transport studies up to now, due to two reasons: on one hand, multiwall carbon nanotubes appear to be strongly doped, which requires too high gate voltages for depletion. On the other hand, conventional backgate techniques using degenerately doped Si/SiO_2 layers provide only a weak capacitative coupling of the gate electrode to the tube due to the large distance of $\sim$100 nm. Thus, in this work the Si backgate has been replaced by a highly effective Al/Al_2O_3-layer. This provides a drastically larger coupling, since the distance is determined only by the thickness of the native oxide ($\sim$ 3 nm). Additionally, the oxide has a high dielectric constant $\epsilon \sim$10, compared to SiO_2 ($\epsilon \sim$2).

5.2 Preliminary Measurements

Electronic transport measurements at low temperatures have been performed for a single multiwall nanotube with diameter 28 $\pm$1 nm and a length of 2.1 $\pm$0.1 μm. The sample has been produced by spanning the nanotube across a Al gate finger by the use of high frequency electric fields, as described in Sec. 4.3. The spacing between the Au contact electrodes was 400 nm. Fig. 5.1 shows the linear response resistance R as a function of the Al backgate voltage for temperatures ranging from 40 K down to 1.7 K in zero magnetic field and gate voltages between -3 V and 2 V.

An aperiodic fluctuation pattern in R arises with decreasing temperature. This pattern has previously been interpreted as universal conductance fluctuations (UCF) [3], which are thermally averaged as temperature is increased. The conductance fluctuations as a variation of gate voltage arise from the shift of the Fermi wave length in a static scattering potential.
As described in Sec.3.1.3, the root-mean-square amplitude δG_{rms} of fluctuations allows us to extract the phase coherence length L_φ. If L_φ is smaller than both the

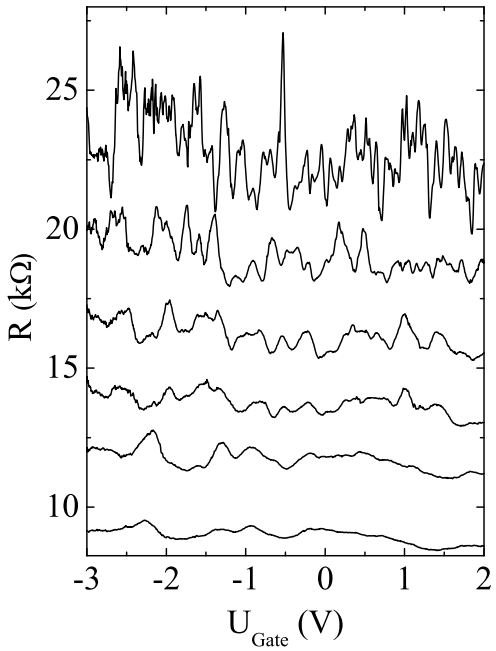

Figure 5.1: Two-terminal resistance of a single MWNT as a function of gate voltage for temperatures of 1.7, 5, 10, 15, 20 and 40 K from top to bottom. The curves are offset for clarity.

contact spacing and the thermal length $L_T = (D\hbar/k_\mathrm{B}T)^{1/2}$, where D is the diffusion constant, then $\delta G_\mathrm{rms} = \sqrt{12}(e^2/h)(L_\varphi/L)^{3/2}$, as given in Eq. 3.12. This way, one obtains L_φ as a function of temperature. The result is shown in Fig. 5.2. Note that for the scenario $L_T \ll L_\varphi \ll L$, the temperature dependence of δG_rms is given by Eq. 3.13. From this, $L_\varphi \propto \delta G_\mathrm{rms}^2 T$ follows. Inserting the measured values for δG_rms would result in an (unphysical) increase of L_φ with temperature, and hence this regime can be ruled out.

These first measurements allow the estimation of mesoscopic lengthscales present in the tube. Fig. 5.2 shows that L_φ is smaller than 120 nm for $T > 2$ K. This implies that $W < L_\varphi < L$, where W and L is the tube width and the contact spacing, respectively. Hence, phase coherence is preserved over the tube width and the electronic transport is effectively quasi-one-dimensional. Note that above 3 K, L_φ is smaller than the tube circumference, which is an important fact for Aharonov-Bohm type experiments.

The temperature dependence of L_φ gives insight into the dephasing mechanism. For Nyquist dephasing, $L_\varphi \propto T^{-1/3}$ is predicted (see Sec. 3.2.1). This behavior is sketched in Fig. 5.2 as a line fit. For temperatures above 5 K, the data agree fairly well with theory. The exact functional form (Eq. 3.17) enables us to estimate the

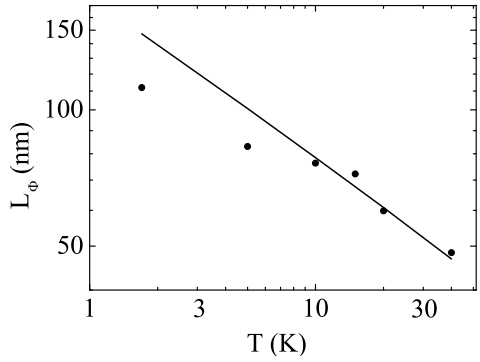

Figure 5.2: Temperature dependence of the phase coherence length derived from weak localization measurements (dots). Line: $T^{-1/3}$ power law fit to the data points above 10 K.

diffusion constant $D \approx 70$ cm^2/s and, using the Fermi velocity $v_F = 10^6$ m/s, the elastic mean free path $L_{el} = 2D/v_F \approx 10$ nm. The thermal wavelength turns out to be of the order 180 nm at 2 K and 40 nm a 40 K. This leads to the conclusion that electronic transport in MWNTs is diffusive or, at best, quasiballistic.
Fig. 5.3 shows a gate sweep of the same sample under similar conditions, but measured one day later. Thermal cycling to about 80 K results in significant changes of the gate characteristics compared to 5.1, which is a typical signature of UCF. It indicates a partial scrambling of the interference pattern by thermally activated motion of scatterers between two cooldowns.
Magnetoresistance (MR) traces provide information on both quantum interference and the electronic bandstructure of MWNTs, since their shape is predicted to depend strongly on both the contribution of weak localization (see section 3.1.1) and the (field dependent) density of states.
In order to obtain a first impression, MR curves have been taken for various fixed gate voltages and perpendicular fields from -10 to 10 T at a temperature of 1.7 K. The values of the gate voltage are marked as arrows in the left panel of Fig. 5.3. Note that the field sweeps have been performed at gate voltages corresponding to UCF peaks and dips as well as intermediate points. The resulting set of MR curves is also plotted in Fig. 5.3. Each curve reveals a symmetric peak in the MR located at $B = 0$ T. This negative MR can be well explained in terms of weak localization (WL) [3, 43]. The characteristic field for the suppression of WL has a value of about 1 T for all curves in Fig. 5.3. The peak amplitude is varying with gate voltage. This implies that the phase coherence length is not a constant, but rather also depends on the gate voltage and hence the Fermi energy.

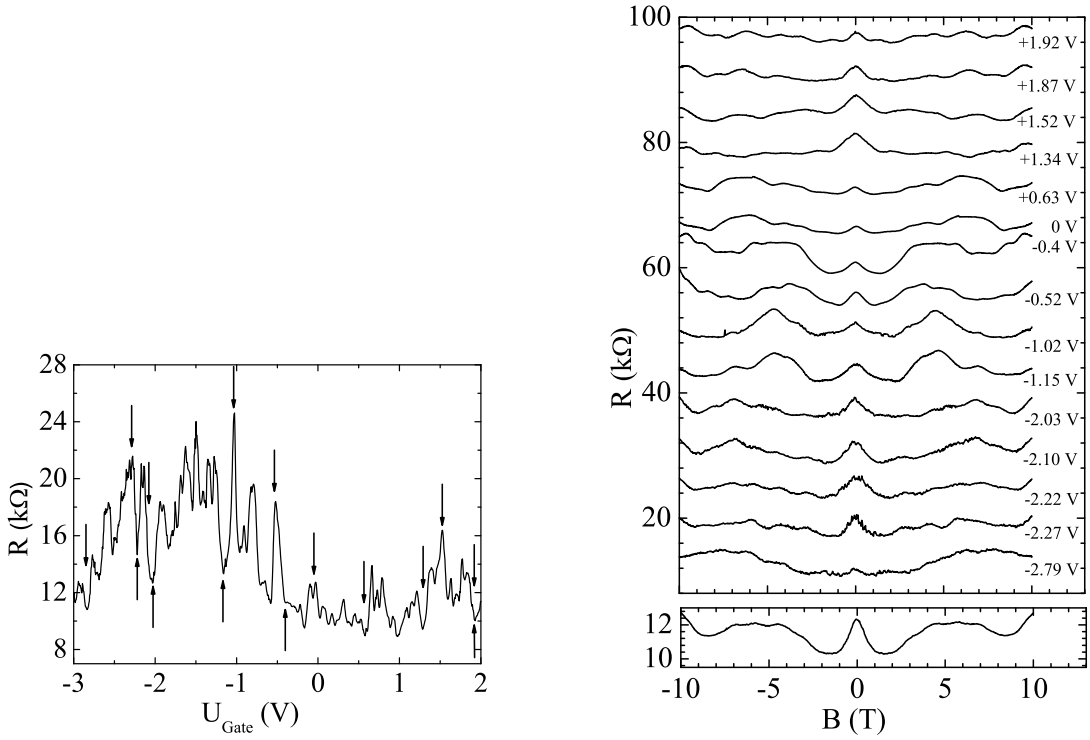

Figure 5.3: Left: Gate sweep after thermal cycling to 300 K of the same MWNT as in Fig. 5.1. The temperature was $T = 1.7$ K. The arrows indicate the positions of the magnetic field sweeps shown in the right figure. Right, upper panel: Magnetoresistance at $T = 1.7$ K. Different voltages were applied to the Al backgate and the magnetic field was applied perpendicular to the tube axis. The curves are offset for clarity. Lower panel: Ensemble average of all magnetoresistance traces.

For higher fields aperiodic fluctuations appear, which again resemble UCFs. A closer look at these oscillations reveals that peaks in the MR primarily appear that correspond to enhanced backscattering, while comparable dips are absent in the investigated ranges of magnetic fields and gate voltages. Each value of the gate voltage, and hence the Fermi level of the tube, corresponds to a different Fermi wave length and thus a change of the phase shifts between the different scatterers. Provided that the change in gate voltage, and hence in E_{F}, is sufficiently large, a complete scrambling of the interference pattern can be achieved. The magnetofingerprints of adjacent peaks and dips sometimes show a similar magnetofingerprint, differing mainly in the average resistance. The latter seems to be more sensitive to small changes of the gate voltage than the pattern of the magnetofingerprint itself. Hence, the oscillations also might originate from the nanotube bandstructure. This

behavior may be caused by the effect of a transversal magnetic field on the density of states and hence the MR, as discussed in Ref. [9].
The ensemble average over all MR curves is plotted in the lower panel of Fig. 5.3. In this curve, all UCF contributions are expected to average out. The zero field peak remains, as well as the high resistance region between 3 and 6 T. This leads to the assumption that both weak localization and bandstructure effects have to be considered.
In conclusion, the preliminary measurements revealed the necessity for a systematic and detailed investigation of the (inter)action of the MWNT bandstructure and the quantum interference. This has to be achieved by low temperature measurements in magnetic fields both parallel and perpendicular to the nanotube axis. Thereby, the highly efficient gate can be used to cover a large fraction of the electron energy spectrum.

Chapter 6

Bandstructure Effects in Multiwall Carbon Nanotubes

In this section conductance measurements on multiwall carbon nanotubes in a perpendicular magnetic field are reported. An Al backgate with large capacitance is used to considerably vary the nanotube Fermi level. This allows to search for signatures of the unique electronic band structure of the nanotubes in the regime of diffusive quantum transport. We find an unusual quenching of the magnetoconductance and the zero bias anomaly in the differential conductance at certain gate voltages, which can be linked to the onset of quasi-one-dimensional subbands.
The present section has been submitted for publication in *Physical Review Letters*.

6.1 Gate Efficiency and Transport Regimes

The samples, as used for the measurements in this section, are prepared by random dispersion of multiwall carbon nanotubes on prepatterned Al gate fingers and subsequent contacting with Au, as described in Section 4.2. Two-terminal conductance measurements were carried out for two samples, called 'A' and 'B' in the following. The lengths of the samples are 5 μm and 2 μm and their diameters are 19 nm and 14 nm, respectively. A scanning electron micrograph of sample B is presented in Fig. 6.1. In order to characterize the dependence of the differential conductance of sample A on the gate voltage U_{Gate}, a small ac bias voltage of 2 $\mu\mathrm{V} \ll k_{\mathrm{B}}T$ was applied and the current was measured at several temperatures T. Fig. 6.1 shows the conductance G as a function of U_{Gate} at 300 K, 10 K, 1 K and 30 mK. The conductance at room temperature exhibits a shallow minimum located at $U_{\mathrm{Gate}} \approx -0.2$ V. The position of the conductance minimum can be attributed to the charge neutral-

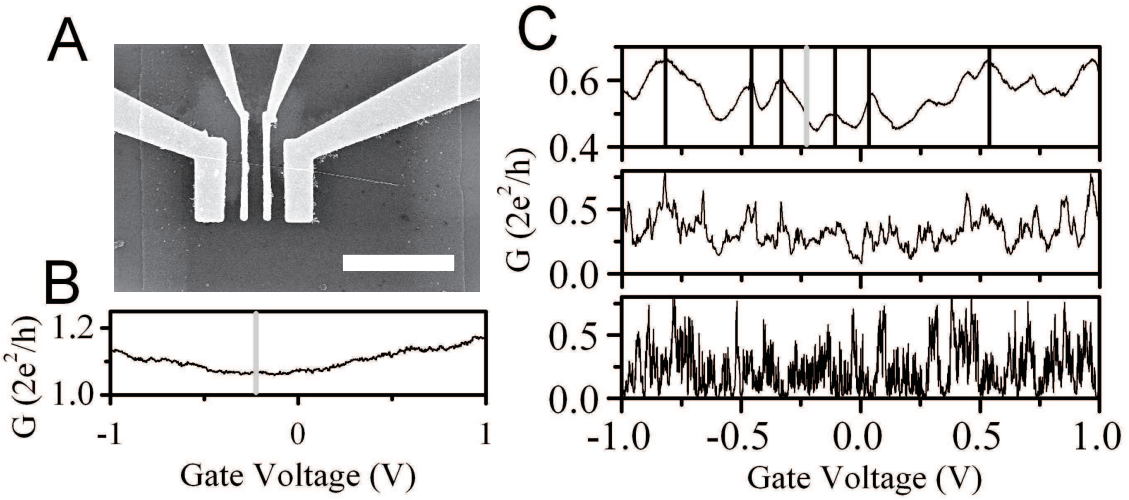

Figure 6.1: (A) Scanning electron micrograph of sample B: an individual multiwall nanotube is deposited on a prestructured Al gate electrode and contacted by four Au fingers, which are deposited on top of the tube. The electrode spacing is 300 nm. For the measurements, only the two inner electrodes are used. The scalebar corresponds to 2 μm. Note that on the right outermost electrode, a second tube has atached to the tube under inspection. (B) Conductance G of sample A as a function of the gate voltage in units of the conductance quantum $2e^2/h$ for 300 K. The estimated position of the charge neutrality point (CNP) corresponds to the minimum of conductance and is indicated. (C) Same as in (B), but for 10 K, 1 K and 30 mK (top to bottom). For the 10K curve, both the positions of the CNP (grey line) and the regions of quenched magnetoconductance (black lines) as observed in Sec. 6.3 are indicated.

ity point (CNP), where bands with positive energy are unoccupied while those with negative energies are completely filled (see also the results of Krüger *et al.* , Ref. [31]). When the Fermi level is tuned away from the CNP, more and more subbands can contribute to the transport and an increase of the conductance is expected. This matches well with the experimental observation and reveals the high efficiency of the gate as well as an intrinsic n-doping of the tube. Note that apart from this work no systematic transport studies for multiwall carbon nanotubes in the vicinity of the charge neutrality point could be performed, mainly due to the small capacitance between the nanotubes and the conventional Si backgate. The location of the minimum varied from sample to sample. We observed p- as well as n-doping at $U_{\mathrm{Gate}} = 0$ V in several samples.

The $G(U_{\mathrm{Gate}})$ curves in Fig. 6.1 show an increasing amplitude of the conductance fluctuations as the temperature is lowered, while the average conductance decreases.

At 30 mK, the current through the sample is completely suppressed for many values of the gate voltage. This can be interpreted as a gradual transition from a coexistence of band structure effects, universal conductance fluctuations and charging effects at 10 K and 1 K to the dominance of Coulomb blockade at 30 mK. These transport features do not show up independently of each other. Nevertheless, the variation of temperature enables us to study the samples in the dominant presence of a single regime.

6.2 Irregular Coulomb Blockade

As described in Sec. 3.2.3, at the lowest temperatures a first approximation of a single nanotube with two contacts and a gate electrode is given by the model of a single electron transistor (SET). Recording the differential conductance as a function of both the bias voltage V_{bias} and the gate voltage U_{gate} allows to extract information on the charging energy and the capacitances of the system. Such measurements were performed for both samples, A and B. The result for sample A in a small interval of gate voltage ranging from -40 to 100 mV and for dc bias voltages of ± 0.8 mV are presented in Fig. 6.2. As already indicated by the linear-response conductance

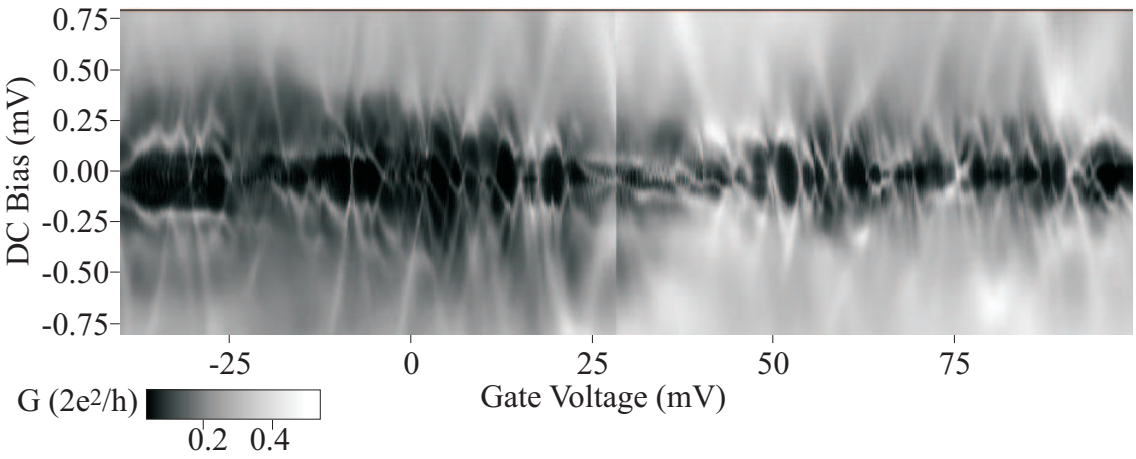

Figure 6.2: Greyscale coded conductance as a function of gate voltage and dc bias voltage. Blue regions correspond to current suppression, while red regions indicate high current.

curve for a temperature of 30 mK (see Fig. 6.1), an irregular pattern of regions occurs, where current is suppressed ("Coulomb diamonds").
The average density of transmission resonances along the U_{gate}-axis is of the order 1000 per Volt, which demonstrates the high efficiency of the Al backgate (see also Sec. 6.4).

The height $\Delta V_{\rm dc}$ of the diamonds varies between ∼0.2 mV and 1 mV. In the SET model, $\Delta V_{\rm dc}$ measures the charging energy $E_{\rm ch}$ and the level spacing δE (see Section 3.2.3).

$$\Delta V_{\rm dc} = \frac{4E_{\rm ch}}{e} + 2\delta E. \tag{6.1}$$

For a one-dimensional dot with length L and one linear electronic band with Fermi velocity $v_{\rm F}$, δE is given by

$$\delta E = \frac{hv_{\rm F}}{2L}. \tag{6.2}$$

Using $v_{\rm F}$=10^6 m/s (graphite) and the tube length of 5 μm, we obtain δE=0.4 meV. Hence, at the largest diamonds, the level spacing originating from the finite length of the nanotube may be involved, while the vast majority of the features indicate a high density of levels (i.e. δE=0).

The width $\Delta U_{\rm gate}$ takes values between ∼1 mV and 4 mV. Within the SET model, this corresponds to gate capacitances $C_{\rm gate}$=$e/U_{\rm gate}$ ranging from 40 aF to 160 aF. This is only a fraction of the sum capacitance $C_\Sigma = C_{\rm gate} + C_{\rm leads}$, which will turn out to be of the order 1500 aF (see Sec. 6.4).

The irregularity of the pattern, as well as the small capacitances, show that transport does not occur through a single quantum dot of constant size. It suggests that the tube decomposes into a series of dots due to defects and/or disorder. Such a behavior has also been observed in singlewall tubes by other groups [49]. If only single-electron tunneling is considered, the serial-dot model predicts a vanishing conductance near zero dc bias for all gate voltages, because the dots cannot be simultaneously driven into transmission. This is indeed the case for the singlewall tubes (see Ref. [49]), while in our measurement regions with high zero-bias conductance are present. Therefore, strongly coupled dot series as well as transport by higher order tunneling processes must be considered, in order to explain the observations at least qualitatively.

In Fig. 6.3, the differential conductance is plotted as a function of gate voltage $U_{\rm gate}$ and a magnetic field B perpendicular to the tube axis. The gate region matches the one depicted in Fig. 6.2. As can be seen from the graph, some Coulomb blockade peaks show a shift with increasing magnetic field, especially in the region $U_{\rm gate}$ = 0...25 mV. This behavior has been attributed to the Zeeman splitting originating from even/odd filling of a quantum dot [50]. Again, the conductance pattern is irregular. It includes field dependent transitions from well defined transmission resonances to large conducting regions and vice versa. This is another indication for the presence of strong disorder, which leads to a change of the level structure by the magnetic field.

At this point, one can ask for the origin of the disorder potential, which creates a decomposition of the tube into strongly coupled segments. One of the possible

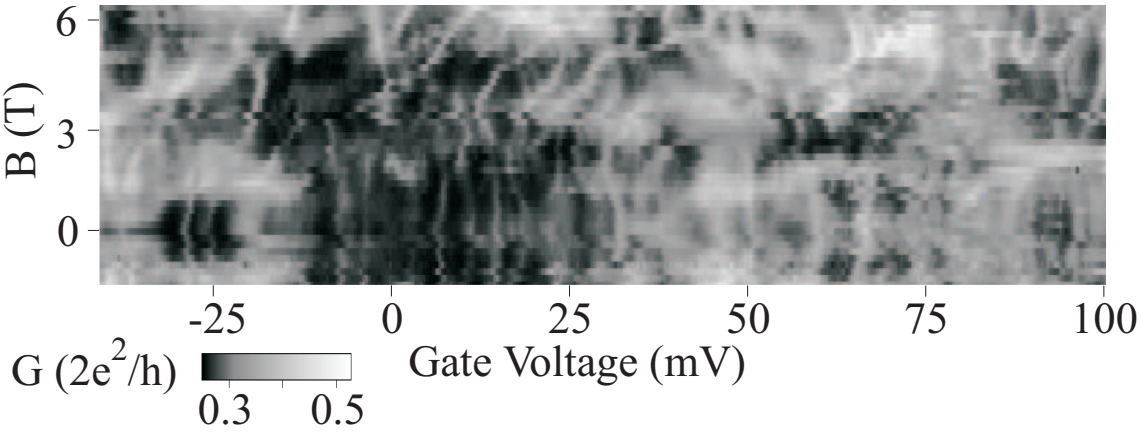

Figure 6.3: Greyscale coded conductance as a function of gate voltage and a perpendicular magnetic field $B = -2...7$ T.

sources is the contact region of the tube and the gate dielectric. The gate layer is not grown epitactically, but rather has a granular surface. The average grain size amounts ~ 30 nm, which is of the same order as the estimated quantum dot dimensions. These problems can be overcome by preparing freely suspended nanotubes, at the cost of a decreased gate efficiency. Nevertheless, future experiments of this kind are highly desirable, for a deeper insight into the quantum dot behavior of multiwall carbon nanotubes.

6.3 Magnetoconductance

In order to explore the interplay between the bandstructure of the nanotube and quantum interference effects, the differential conductance G has been measured as a function of the gate voltage U_{gate} and a magnetic field B perpendicular to the tube. B was changed in steps, while U_{gate} was swept continuously. Fig. 6.4 shows the results for sample A at temperatures of 1 K, 3 K and 10 K in a greyscale representation. We have checked for several gate voltages that $G(B)$ is symmetric with respect to magnetic field reversal as required in a two point configuration (not shown). In addition, most of the curves show a conductance minimum at zero magnetic field. A closer look at the data reveals that both the amplitude and the width of the conductance dip vary strongly with gate voltage. The "frequency" of this modulation with gate voltage increases with decreasing temperature. As shown in the previous section, the conductance fluctuations at low temperatures are caused to a large extent by Coulomb blockade. In addition, universal conductance fluctuations are also superimposed, whose amplitude also grows as temperature is lowered (see Section 3.1.3). Hence, the search for bandstructure effects seems most rewarding at higher

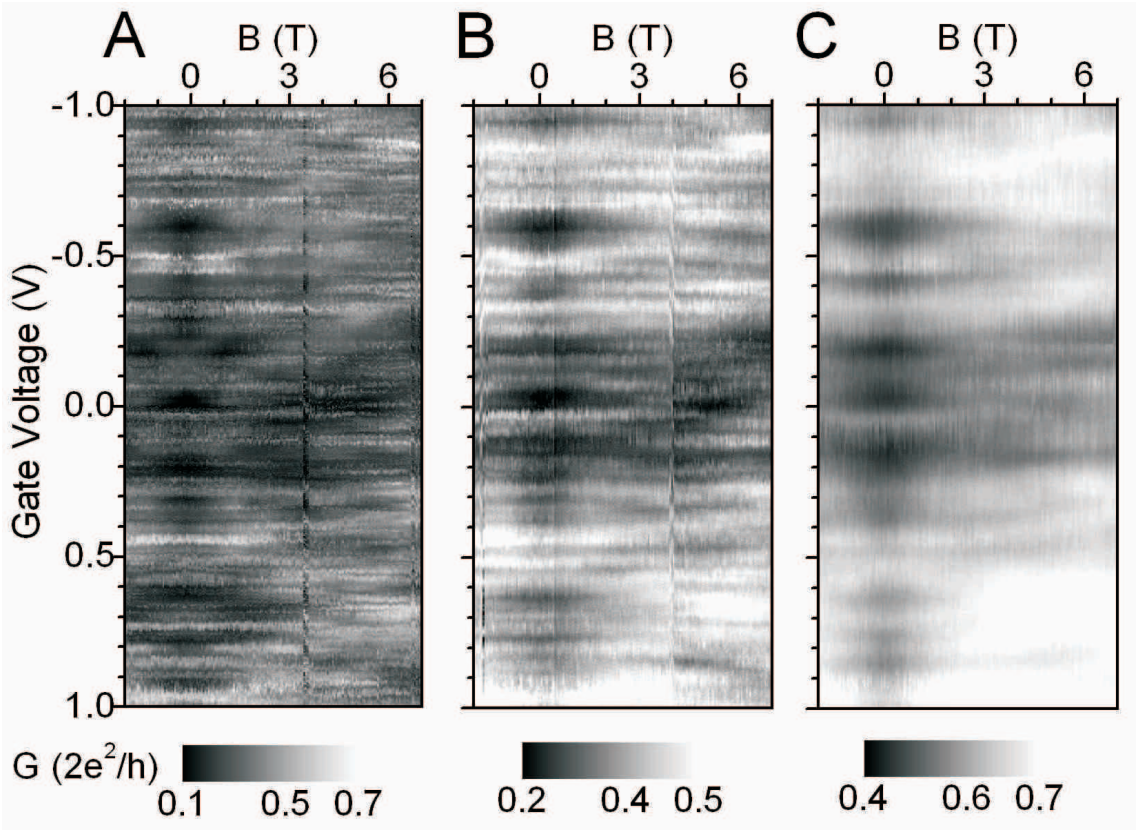

Figure 6.4: Greyscale representation of the differential conductance dI/dV of sample A as a function of the gate voltage and the magnetic field B at 1 K (A), 3 K (B) and 10 K (C). Dark regions correspond to low conductance and white regions to high conductance.

temperatures, i.e. 10 K or more, since there Coulomb blockade is nearly lifted, while bandstructure effects should still be present.

In order to make the variation of the magnetoconductance with gate voltage more visible, we subtracted the curve at zero magnetic field (see Fig. 6.1) from all gate traces at finite fields. The deviation from the zero-field conductance at T=10 K is presented as a greyscale plot in Fig. 6.5A. Fig. 6.5B shows the result of this procedure for sample B at T=17 K. The most striking observation is that the magnetoconductance (MC) nearly disappears at certain gate voltages U^*, as indicated by arrows. These voltages U^* are grouped symmetrically around the conductance minimum at $U_{\mathrm{gate}} \approx -0.2$ V (sample A) in Fig. 6.1, which we have assigned to the charge neutrality point (CNP). The position of the CNP, as well as the gate voltages of MC quenches have been indicated also in the linear response conductance curve (Fig. 6.1) by grey and black vertical lines, respectively. The latter always coincide with conductance maxima. Sample B shows an equivalent behavior: here the MC quenches are also grouped symmetrically around the CNP, which is located

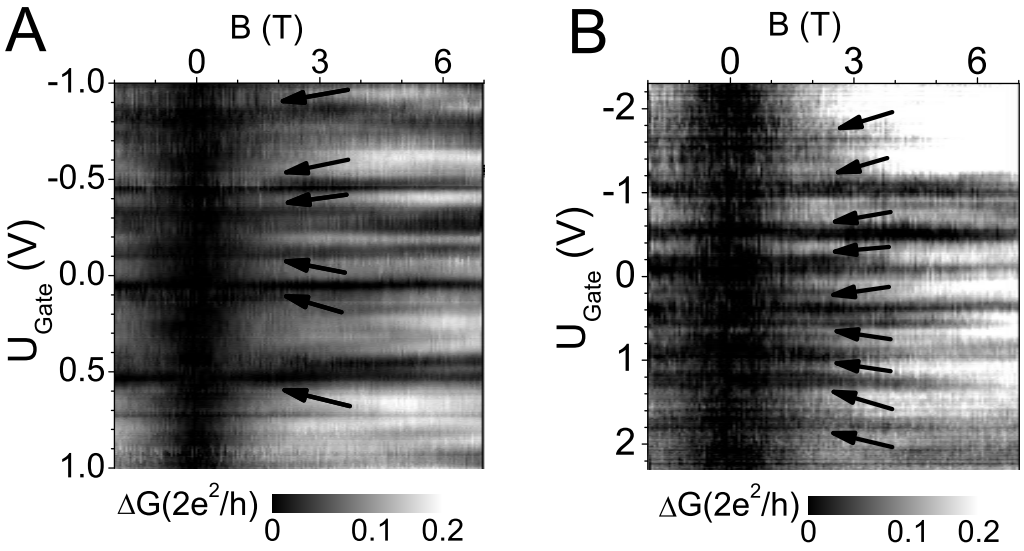

Figure 6.5: (A) Greyscale plot of the deviation of the conductance G of sample A from the zero-field conductance as a function of the gate voltage U and the magnetic field B: $\Delta G(U,B) = G(U,B) - G(U,0)$. Arrows indicate the regions of quenched magnetoconductance. (B) Same for sample B.

at $U_{\mathrm{gate}} = +0.5$ V.
These observations lead us to the conjecture that the quenched MC may occur at the onset of subbands of the outermost nanotube shell, which is believed to carry the major part of the current at low temperatures [45]. This is supported by the argument that in the present experiment the tube is contacted by finger electrodes, which are only in contact with the outermost shell.

6.4 Relation to Electronic Bandstructure

To confirm the idea of a quenched magnetoconductance at the subband onsets, a simple bandstructure model is applied. The black line in Fig. 6.6A shows the density of states of a singlewall (140,140) armchair nanotube in the light-cone approximation (see Sections 2.1, 2.4), which matches the diameter of sample A (19 nm). Typical van Hove singularities arise at the energies, where the subband bottoms are located [47]. By integration over energy one obtains the number ΔN of excess electrons on the tube, plotted as a grey line in Fig. 6.6 for the parameters of sample A. In this

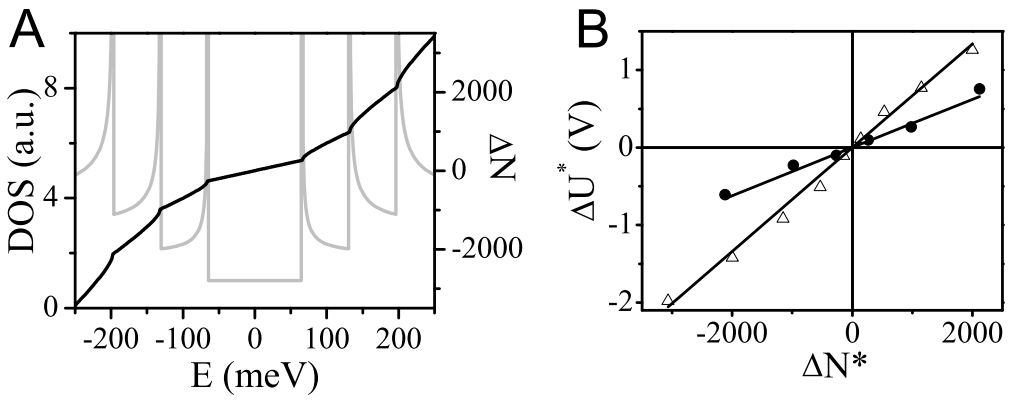

Figure 6.6: (A) Calculated π-orbital density of states (DOS) for a (140,140) armchair nanotube of diameter of 19 nm (grey line) as a function of energy. Number of excess electrons $N(E)$ (black line) as obtained from the integration of the DOS from 0 to E. The subband spacing for this diameter is 66 meV. (B) Measured gate voltage values ΔU^* of nanotube subband onsets vs. calculated numbers of electrons ΔN^* at subband onsets for sample A (circles, diameter 19 nm) and B (triangles, diameter 14 nm). The lines correspond to linear fits of the data. The slopes of the lines correspond to gate capacitances per length of 300 aF/μm and 330 aF/μm for sample A and B, respectively.

way, we can determine the number ΔN^* of electrons at the onset of the nanotube subbands. If we assume as usual a capacitative coupling between the gate and the tube, ΔN can be converted into a gate voltage via

$$CU_{\mathrm{Gate}} = e\Delta N. \tag{6.3}$$

In Fig. 6.6 the measured gate voltages U^* of quenched magnetoconductance are plotted versus the calculated ΔN^* for both samples. Both data sets fit very well into straight lines, which demonstrates that most of the positions U^* of the quenched magnetoconductance agree very well with the expected subband onsets. In addition, the gate capacitances C are provided by the slope of U^* vs. ΔN^*. The capacitances per length are nearly identical, i.e. 300 aF/μm and 330 aF/μm for samples A and B, respectively. These values agree astonishingly well with simple geometrical estimates of C, indicating the consistency of the interpretation[1]. From the capacitance C and the calculated dependence of the number of electrons N on energy, one can convert the gate voltage into an equivalent Fermi energy. For sample A, the first line

[1]Modelling the system as a plate capacitor gives a capacitance of C=$\varepsilon_0\varepsilon_{Al_2O_3}A/d$. Inserting $\varepsilon_{Al_2O_3}\approx$9, $A = 14\mathrm{nm}\times 1\mu\mathrm{m}$ (tube diameter $\times$ unit length) and d=3 nm (oxide thickness) results in C_{gate} =370 aF/μm for sample B.

of quenched magnetoconductance is equivalent to the subband spacing of 66 meV with respect to the CNP (see Sec. 2.4), the second line corresponds to 2×66 meV, and so on. For sample B, the subband spacing is 89 meV.
From the above discussion, the interpretation of the flat regions in the magnetoconductance as a "fingerprint" of the bandstructure of the outermost nanotube shell seems reasonable. Nevertheless, many questions remain. For example, one can ask why the differential conductance does not show steps, since this would be exactly the behavior of a few-channel ballistic conductor, whose transport channels are opened one by one by means of a gate voltage. Such anomalies could come from the disorder in the system. Hence, questions of this kind represent a motivation for a closer look at the quantum interference properties of the tube, which will be done in the following sections.

6.5 Contribution of Weak Localization

The typical dip in the magnetoconductance at $B = 0$ in Fig. 6.4 has been observed earlier and can be explained in terms of quasi one-dimensional weak localization in absence of spin-orbit scattering [3, 44, 33]. The weak localization correction ΔG_{WL} to conductance provides information on the phase coherence length L_φ of the electrons. With W being the measured diameter and L the electrode spacing of the nanotube ($L = 300$ nm for both samples), ΔG_{WL} is given in the quasi-one-dimensional case ($L_\varphi > W$) by

$$\Delta G_{\mathrm{WL}} = -\frac{e^2}{\pi\hbar L}\left(\frac{1}{L_\varphi^2} + \frac{W^2}{3\ell_m^4}\right)^{-1/2}, \tag{6.4}$$

where $\ell_{\mathrm{m}} = (\hbar/eB)^{1/2}$ is the magnetic length (see Sec. 3.1.1 and Ref. [18]). In Fig. 6.4 each row displays a dip around zero magnetic field, where both the amplitude and the width of the dip vary strongly with gate voltage. Here the question arises, to which extent the properties of the conductance dip can be described by weak localization. Thus, we have used the weak localization expression above to fit the low field magnetoconductance with L_φ and $G(B = 0)$ as free parameters. The conductance ΔG_{WL} as calculated using the fit parameters is plotted in Fig. 6.7B and D for sample A and B, respectively. Three representative magnetoconductance traces for sample A, together with fitted curves are presented in Fig. 6.7A. For both samples, we find that conductance traces are reproduced very well by the fit for fields up to 2 T. For higher fields deviations occur, most probably due to residual universal conductance fluctuations and modifications of the density of states (DoS) by the magnetic field. The properties of a magnetic field-dependent DoS will be addressed

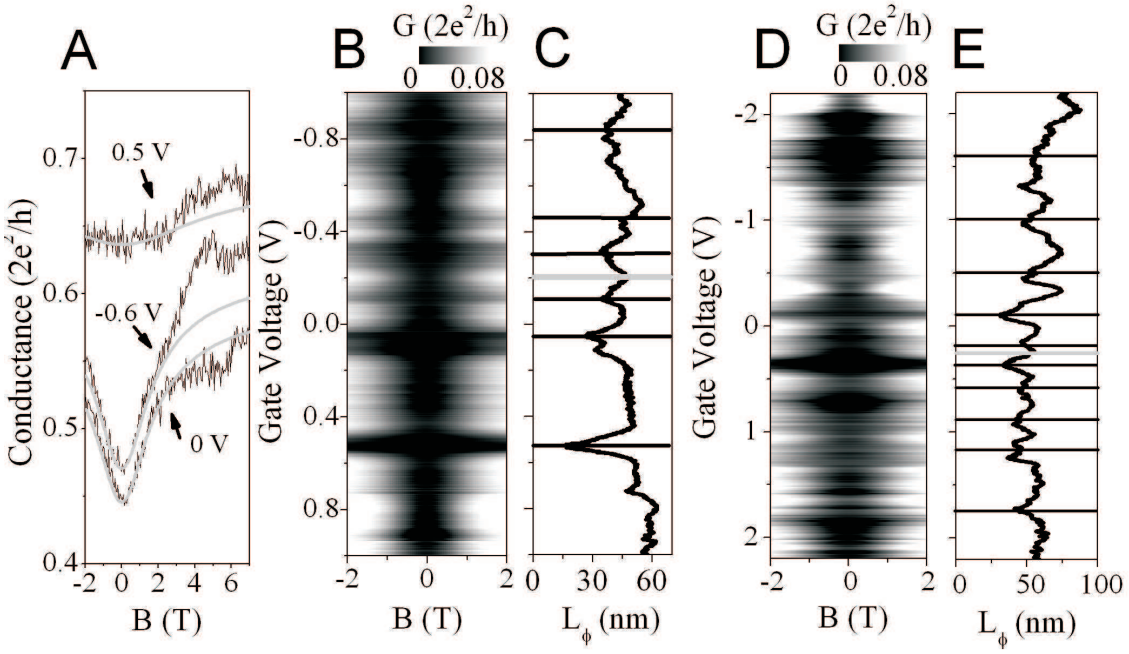

Figure 6.7: (A) Black lines: representative magnetoconductance traces of sample A at gate voltages U=0.5 V, -0.6 V and 0 V (top to bottom). Grey lines represent 1D weak localization fits. (B) Reproduction of the magnetoconductance of sample A by 1D weak localization fits. The parameters L_φ and $G(B = 0)$ are used as obtained by fitting the data in Fig. 6.4. (C) Phase coherence length L_φ vs. gate voltage as obtained from the fit for sample A. The positions of the charge neutrality point (grey line) and the regions of quenched magnetoconductance (black lines) are indicated. (D) and (E): same for sample B, but at 20 K.

in Chap. 7. In this way, we obtain an energy dependent phase coherence length $L_\varphi(E_\mathrm{F})$, which is also plotted in Fig. 6.7. L_φ varies from 20 to 60 nm (sample A) and from 30 to 90 nm (sample B), respectively. It turns out that L_φ displays pronounced minima which correspond to the regions of nearly flat magnetoconductance in Fig. 6.5. The positions of the minima are marked in Fig. 6.7 (black lines), as well as the CNP (grey line). From the preceding discussion, we can say that weak localization seems to be suppressed at the onset of nanotube subbands.

6.6 Dephasing Mechanism

Studies of the magnetoconductance at different temperatures allow an insight into the temperature dependence of the phase coherence length. This, in turn, gives

indications for the main inelastic scattering processes involved.
In former experiments, quasielastic electron-electron scattering has been identified as the dominating dephasing mechanism [3, 39, 44]. Dephasing by electron-phonon

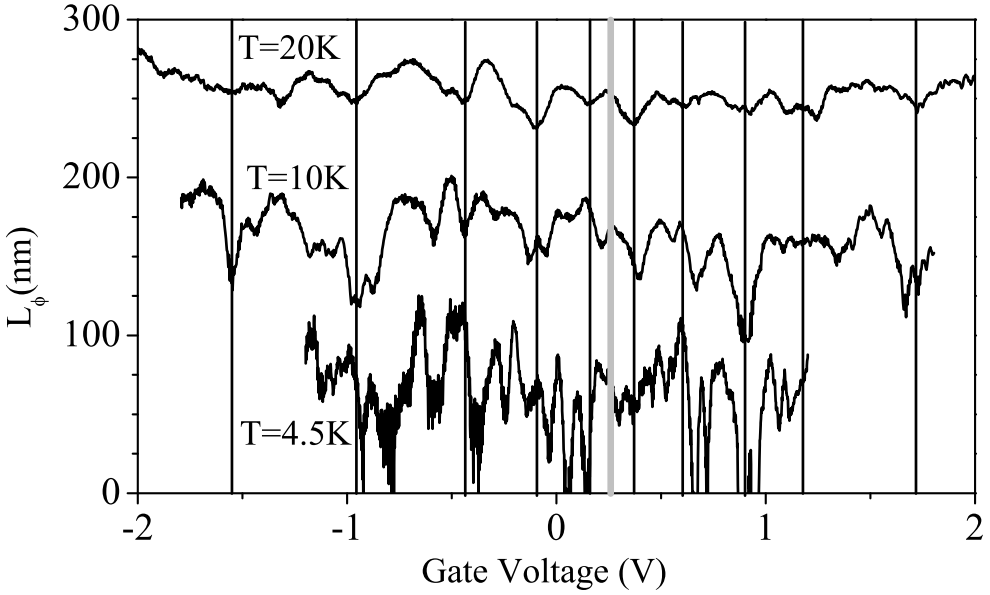

Figure 6.8: Phase coherence length L_φ vs. gate voltage for sample B as obtained from weak localization fits at 20 K, 10 K and 4.5 K (top to bottom). Note that the curves for 10 K and 20 K are offset by 100 nm and 200 nm, respectively. Lines denote the positions of the subband onsets (black) and of the charge neutrality point (grey).

scattering is negligible since the corresponding mean free path exceeds 1 μm even at 300 K [51, 52]. The theory by Altshuler, Aronov and Khmelnitzky [26] predicts

$$L_\varphi = \left(\frac{GDL\hbar^2}{2e^2 k_\mathrm{B} T} \right)^{1/3}, \tag{6.5}$$

where G is the conductance, D is the diffusion constant and L is the contact spacing (see also Sec. 3.2.1). Thus, electron-electron-scattering dominates if L_φ depends on temperature via $L_\varphi \sim T^{-1/3}$.
The magnetoconductance measurements have been repeated for temperatures ranging from 1 K to 60 K and for both samples, cf. Fig. 6.4. The fitting of weak localization behavior, as described in the preceding section, gives values for $L_\varphi(U_\mathrm{gate}, T)$. The result for sample B at temperatures 4.5 K, 10 K and 20 K is shown in Fig. 6.8. For all temperatures, L_φ diplays a strong modulation with gate voltage. As discussed above, the dips of L_φ at certain gate voltages correspond to the onset on the

nanotube subbands. These gate voltages are marked with lines in Fig. 6.8 as well as the CNP. The variation amplitude of L_φ increases with decreasing temperature. Additional features arise, which come most probably from charging effects and universal conductance fluctuations. Note that the average L_φ is at least of the order of the tube circumference for all investigated temperatures, which corresponds to quasi-one-dimensional quantum transport.

The large variation of L_φ makes it hard to determine its detailed temperature dependence as a function of the gate voltage. Instead, the average of the magnetoconductance traces for all gate voltages has been performed for each temperature. As described in Chapter 5, with this method an ensemble average is done, where the contribution of universal conductance fluctuations is averaged out. The results at 1 K, 3 K, 10 K and 60 K are presented in 6.9. For the comparison of the curves

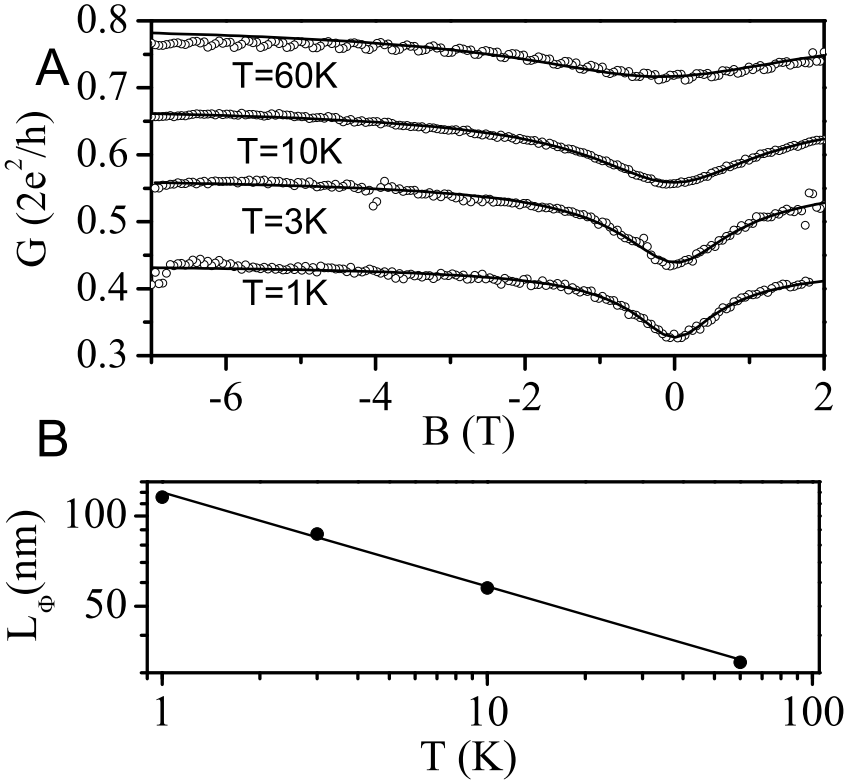

Figure 6.9: (A) Averaged magnetoconductance of sample A (circles) at temperatures of 60 K, 10 K, 3 K and 1K (top to bottom) and fits of 1D weak localization behavior (lines). (B) Double-logarithmic plot of the temperature dependence of the phase coherence length L_φ as obtained from the weak localization fit (black dots). The red line corresponds to a power law fit with an exponent -0.31.

with theory, one has to bear in mind that the average runs also on curves with suppressed MC. Hence, for the fit an averaged weak localization contribution of the form $\Delta G^*_{\mathrm{WL}} = A \cdot \Delta G_{\mathrm{WL}}$ with a scaling factor $0 < A < 1$ has been taken into account. Strictly speaking, this procedure is only correct for the case that $L_\varphi(U_{\mathrm{gate}})$ only assumes two values, namely L_φ and 0. Otherwise, it serves as a good approximation for the average phase coherence length L_φ. The fitted curves are included in Fig. 6.9. They match the data very well, even up to magnetic fields of 7 T. In Fig. 6.9, also the resulting values $L_\varphi(T)$ are presented. The contribution of the universal conductance fluctuations is completely suppressed by ensemble averaging. The temperature dependence matches a power law with exponent -0.31, which is close to the theoretical prediction of $-1/3$. This leads to the conclusion, that the main dephasing mechanism is indeed quasielastic electron-electron scattering.

6.7 Elastic Mean Free Path

Apart from the phase coherence length L_φ, the most important length scale in diffusive conductors is imposed by the elastic mean free path L_{el}. The knowledge of L_{el} gives a quantitative insight into the actual diffusivity of the system, and hence the efficiency of the disorder. The determination of L_{el} from conductance measurements requires the knowlegde of the number of conductance channels, which participate in transport. Up to now, exactly this condition could not be met for multiwall carbon nanotubes, mainly due to the complex structure of the conductance traces and the too small variation of the Fermi energy. Consider a conductor of length L and transverse dimensions $W \ll L$. In the quasi-one dimensional case $W \ll L_\varphi \ll L$, the conductance in presence of (1D) weak localization is given by

$$G = \frac{2e^2}{h}\left(\frac{NL_{\mathrm{el}}}{L} - \frac{L_\varphi}{L}\right), \tag{6.6}$$

where N is the number of conducting channels [54]. According to Eq. , the total conductance G is composed by the classical Drude conductance, which contains L_{el}, and the weak localization contribution given by L_φ/L.

The analysis of the data in this chapter provides us with knowledge of the conductance $G(U_{\mathrm{gate}})$ and the phase coherence length $L_\varphi(U_{\mathrm{gate}})$, both as a function of the gate voltage U_{gate}. The determination of the nanotube subband positions (see sec. 6.4) gives immediately the number of subbands $N(U_{\mathrm{gate}})$. Thus, Eq. 6.7 allows to calculate $L_{\mathrm{el}}(U_{\mathrm{gate}})$.

The result is presented in Fig. 6.10A for the data from sample A at 10 K. At the subband positions, the number of channels is not assumed to change in sharp

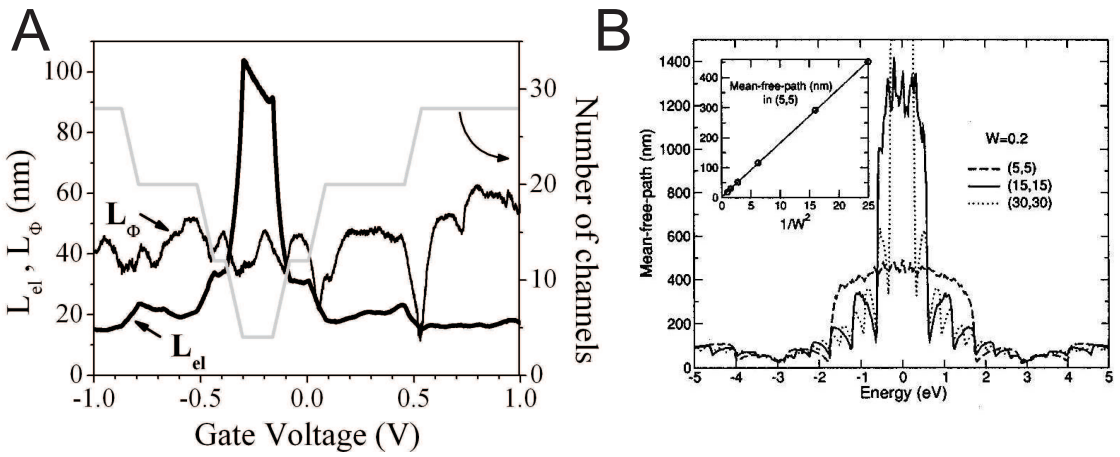

Figure 6.10: (A) Estimated elastic mean free path $L_{\rm el}$, measured phase coherence length L_φ and calculated number of conduction channels vs. gate voltage for sample A at $T = 10$ K. (B) Numerical calculation of $L_{\rm el}$ with Anderson disorder W vs. energy for a (5,5)-tube (dashed line), (15,15)-tube (solid line) and a (30,30)-tube (dotted line) by F. Triozon [53]. Inset: $L_{\rm el}$ at the CNP vs. $1/W^2$ for a (5,5)-tube.

steps. Instead, the band edges were smeared to account for disorder, which is also supported by Ref. [55]. Both the number of channels and $L_\varphi(U_{\rm gate})$ are shown in Fig. 6.10A, as well as the resulting elastic mean free path $L_{\rm el}(U_{\rm gate})$. The fact that $G(U_{\rm gate})$ varies only weakly implies that $L_{\rm el}(U_{\rm gate})$ is dominated by the inverse channel number at a given gate voltage, which leads to a maximum at the CNP as well as to a steep decrease at the band edges. Quantitatively, the maximal value of $L_{\rm el}$ amounts $\sim$ 100nm, and it is reduced stepwise to about 10 nm.

Thus, the variation of the Fermi energy drives the system into several transport regimes: Apart from the CNP, transport in the nanotube appears to be diffusive, since $L_{\rm el}$ is much smaller than the nanotube length (the contact spacing is 300 nm), and also smaller than the tube circumference of $\sim$60nm. In the vicinity of the CNP, a quasiballistic regime is entered, where $L_{\rm el}$ exceeds both L_φ and the tube diameter. As a contrast, at some subband edges L_φ drops to values which are comparable to $L_{\rm el}$.

Strictly speaking, the previous analysis only provides a lower limit for $L_{\rm el}$, since the contact resistances are not taken into account. Nevertheless, there are arguments that the latter are indeed well below the quantum resistance of $h/2e^2$. One of them is the weak localization dip of the conductance as a function of the magnetic field, which originates most probably from the sample conductance alone. The amplitude of the dip amounts up to 20 percent of the total conductance (see, e.g. Fig. 6.7). This ratio can only be attained if the contact resistances are low. Otherwise, the ratio would be much lower. Hence, the above analysis provides a reasonable estima-

tion of L_{el}.
The results of this section were predicted by numerical calculations by F. Triozon [53], which are presented in Fig. 6.10B. Here, L_{el} is calculated as a function of the Fermi energy E_{F} for disordered singlewall nanotubes with small diameters. The on-site Anderson disorder W was set to $W \sim 0.6$ eV. Like the measurement, the calculations reveal that $L_{\mathrm{el}}(E_{\mathrm{F}})$ decreases with increasing population of the subbands. In addition, $L_{\mathrm{el}}(E_{\mathrm{F}})$ has pronounced dips at the subband onsets.
It must be stressed that for constant disorder W, L_{el} is predicted to show an unusual energy dependence, namely sharp drops at the subband onsets. This can be attributed mainly to the increased number of scattering channels, as soon as a new subband is populated.
In addition, also L_{el} at the CNP is predicted to to be proportional $1/W^2$, where W is the amplitude of the on-site Anderson disorder in the tube (see inset of Fig. 6.10B). This could be used in order to extract a value for the equivalent Anderson disorder from the measured data and to compare the results from different measurements.

6.8 Zero Bias Anomalies

In the preceding sections, only single particle quantum interference corrections like weak localization have been taken into account, as well as weak electron-electron scattering as a source of dephasing. By the electron-electron-interaction another quantum correction to the conductance is induced and reduces the density of states near the Fermi energy [32]. This leads to a zero bias suppression (the so-called Coulomb gap) in the differential conductance $\mathrm{d}I/\mathrm{d}V$ [46], from which information on the strength of the interaction can be extracted. In the case of tunneling into an interacting electron system with an ohmic environment, the differential conductance $\mathrm{d}I/\mathrm{d}V$ is given by a power law, i.e. $\mathrm{d}I/\mathrm{d}V \propto V^{\alpha}$ for $eV \gg k_{\mathrm{B}}T$, where the exponent α depends both on the interaction strength and the sample geometry [29], see also Sec. 3.2.2. In order to obtain complementary information, we have examined the dependence of the ZBA on the gate voltage U_{Gate}. The differential conductance has been measured as a function of U_{Gate} and V_{Bias} at 10 K. The result is presented in Fig. 6.11 for both samples. For each gate voltage, the conductance shows a dip at zero bias. The zero bias anomaly has a strongly varying width and amplitude with gate voltage and nearly vanishes at the same gate voltages $U_{\mathrm{Gate}} = U^*$ as the magnetoconductance, cf. Fig. 6.11. For each value of the gate voltage, a power law fit for the bias voltage dependence of the differential conductance has been performed. The fit was done in the region $eV \gg k_{\mathrm{B}}T$, since below deviations from the power law behavior occur, in accordance with the theoretical predictions [46]. The resulting

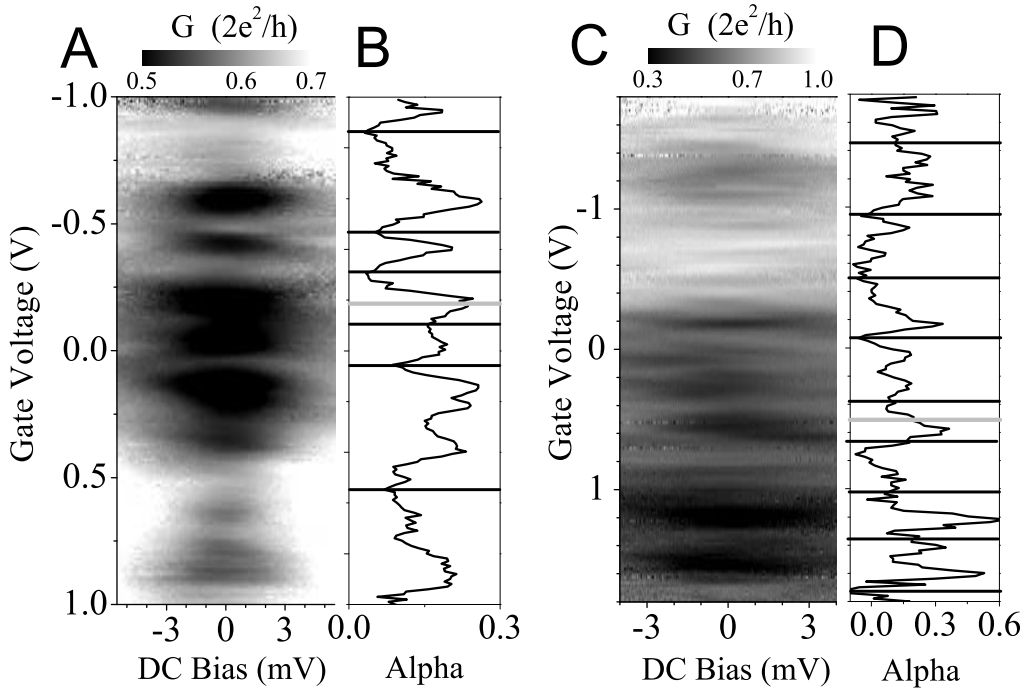

Figure 6.11: (A) Greyscale representation of the differential conductance of sample A as a function of gate voltage and dc bias voltage V_{Bias} at T=10 K. (B) Exponent α vs. gate voltage as obtained from fitting a power law V^{α} to the differential conductance in the range $eV \gg k_{\mathrm{B}}T$. The positions of the charge neutrality point (grey line) and the regions of quenched magnetoconductance (see Fig. 6.5) (black lines) are indicated. (C) and (D): same for sample B.

exponent $\alpha(U_{\mathrm{Gate}})$ is also plotted in Fig. 6.11. For sample A, α varies between 0.03 and 0.3 and shows pronounced minima at the gate voltages U^*. This behavior is in principle also shown by sample B, but here the differential conductance shows offsets and larger deviations from the power law behavior. Since the fitting procedure is less stable in the limit of small exponents, the offsets here lead to (unphysical) negative exponents.

The behavior of the zero-bias conductance $G(U_{\mathrm{gate}}, T)$ with varying temperature allows to extract $\alpha(U_{\mathrm{Gate}})$ in an independent way, since $G \propto T^{\alpha}$ with the same exponent as for the dependence on the dc bias voltage [29]. Thus, the fitting procedure as described above was applied to $G(U_{\mathrm{gate}}, T)$, where T ranged between 3 K and 60 K. The result for sample A is presented in Fig. 6.12A. For comparison, the exponent as obtained from $G(U_{\mathrm{gate}}, V_{\mathrm{bias}})$, is also included. The absolute values of the exponents agree reasonably well within the measurement's accuracy. Both curves display peaks and dips at nearly the same positions. Thus, the results from

the dc bias measurement are confirmed by the temperature dependence.

In summary, the investigation of the differential conductance at both finite dc

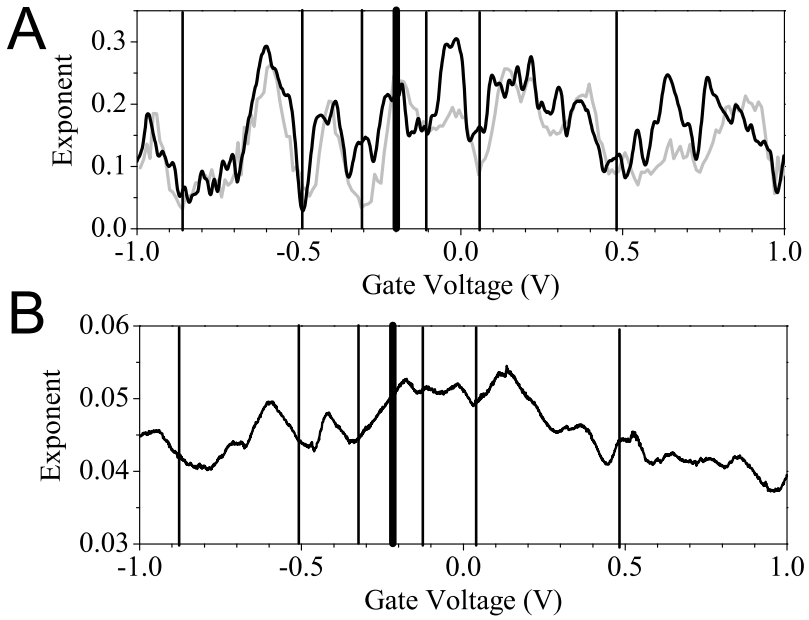

Figure 6.12: (A) Exponent α vs. gate voltage as obtained from fitting a power law V^{α} to the differential conductance in the range $eV \gg k_{\mathrm{B}}T$ for sample A (black line). Grey line: dependence on gate voltage of the power law fit T^{α} for zero bias conductance traces at temperatures ranging from 3 K to 60 K (also for sample A). The positions of the subband onsets and the CNP are included as vertical lines (CNP: bulk line). (B) Exponent α obtained from L_{el} and the number of transport channels.

bias voltages and temperatures lead to the folllowing result: for all gate voltages, a power law in the conductance is observed with an exponent α. This indicates that indeed tunneling into an interacting electron gas occurs. The magnitude of α varies strongly and correlates with the onset of the nanotube subband bottoms. Since α is proportional to the interaction strength g of the electrons, the measurement suggests that g depends on the gate voltage. Weak interaction is present, as soon as a new nanotube subband is populated. Both the variation of g and its low values at the subband bottoms do not agree very well with conventional theoretical approaches. This will be discussed in the following section.

The exponent α allows to be estimated by a different approach. Eq. 3.22 predicts that α is determined by the elastic mean free path L_{el} and the number of transport channels M. Both have been derived for sample A in Sec. 6.7. Thus, α has been

determined and the result is presented in Fig. 6.12B. Qualitatively, the behavior of $\alpha(U_{\mathrm{gate}})$ agrees very well with the results from the other approaches. Quantitatively, in Fig. 6.12B the values for the exponent are smaller by a factor of $\sim$5. From Eq. 3.21, this would mean that the logarithmic term does no more equal unity. Thus, α could be taken as a measure for the interaction strength U_0 of the electrons. From the factor of 5, $\nu_0 U_0 \approx e^5$ is derived, where ν_0 is the noninteracting density of states. Thus, the regime of weak interactions appears to be no more valid.

6.9 Critical Discussion

The experiments in the preceding sections revealed a strong correlation between the single particle interference effects (expressed by the phase coherence length L_φ) and the interaction effects (expressed by the exponent α). Both are strongly reduced at certain positions of the Fermi level, which match well the positions of the van Hove singularities estimated from simple bandstructure models.
At this stage, one can ask to which extent the diffusion properties of the system are influenced by the band structure. Both the results for the elastic mean free path L_{el} (see Sec. 6.7) and numerical calculations by Triozon et al. [53] indicate that L_{el} is not a constant as a function of E_F. L_{el} rather displays a pronounced decrease at the onset of new subbands. At these points strong scattering occurs, resulting from the opening of a highly efficient scattering channel. This has a direct effect on $L_\varphi = \sqrt{D(E_F)\tau_\varphi}$. Of course, τ_φ may also be affected.
Can the energy dependence of $L_{\mathrm{el}}(E_{\mathrm{F}})$ also explain the suppression of the interaction effects? This question has already been raised by Kanda et al. [34], who also observed a pronounced gate modulation of α. For weak electron-electron-interaction the theory of Ref. [32] predicts $\alpha \propto 1/L_{\mathrm{el}}$. This is definitely incompatible with the observed suppression of α at Fermi levels, where diffusion is slow.
The observed strong modulations of L_φ and α are accompanied by a rather weak modulation of the zero bias conductance G at 10 K (see Fig. 6.1). One may thus ask, whether the assumption of weak interactions is valid. From Eq. 6.7, one concludes that for weak modulations of G the increase of the electron density at new subands is apparently compensated by a strong reduction of L_{el}. An equivalent conclusion is derived for the diffusion coefficient D: taking the simple Drude formula

$$\sigma = e^2 \nu(E_{\mathrm{F}}) D(E_{\mathrm{F}}) \tag{6.7}$$

as an orientation, the 'flatness' of G can be explained by a partial compensation of the variation of the electron density ν and D when tuning the Fermi energy E_{F}.

However, a quantitative explanation of the observed interplay between bandstructure effects and quantum corrections to the conductance requires a realistic model calculation for a thick, e.g., (140,140) nanotube including disorder and interaction effects. The simple model of strictly one-dimensional conductance channels is obviously incompatible with the observed weak-localization-like magnetoconductance close to the CNP. The disorder must be strong enough to mix the channels without completely smearing the density of states.

If this interpretation is correct, weak localization should also occur in singlewall nanotubes. Indeed, very recent magnetoconductance measurements by Morpurgo [56] and Bouchiat [57] confirm that this is indeed the case.

In conclusion, the electronic transport measurements on multiwall carbon nanotubes, as presented in this chapter, reveal an interplay of bandstructure effects originating from the geometry of the tube and quantum interference induced by disorder. The results demonstrate the necessity of a systematic theoretical approach which can account both for disorder and bandstructure effects on the same level.

Chapter 7

Aharonov-Bohm Effect and Landau Levels

In this section, electronic transport measurements on individual multiwall nanotubes with large diameter ($\sim$ 30 nm) are reported. Magnetic fields are applied both perpendicular and parallel to the tube axis. The large diameters allow us to study the electronic transport in a regime, where several multiples of the magnetic flux quantum $\Phi_0 = h/e$ penetrate the tube cross section. In addition, an Al backgate is used for a variation of the doping level across several nanotube subbands.
The conductance of the nanotube was recorded as a function of the magnetic field B and the gate voltage U. For parallel fields, both h/e- and $h/2e$-periodic oscillations in the magnetoconductance occur and lead to rhomb-shaped regions of low conductance in the B-U-plane . In the perpendicular case, a region of low conductance forms at small gate voltages, which grows with increasing magnetic field.
The experimental observations are explained well by tight-binding bandstructure calculations for the outermost shell of a multiwall nanotube in a magnetic field.

7.1 Motivation

The cylindrical topology of carbon nanotubes gives rise to several theoretical predictions for the electronic conduction properties in magnetic fields, which are aligned parallel to the tube axis. In terms of diffusive quantum transport, Altshuler-Aronov-Spivak (AAS) oscillations of the conductance with a magnetic flux period of $h/2e$ are predicted [19] for metallic, cylindrical samples. Both the shape and the amplitude of the AAS-oscillations depend strongly on the phase coherence length and the wall thickness. The Aharonov-Bohm effect with a period of h/e is supposed to average

out, since the cylindrical samples can be regarded as many ring shaped conductors in parallel [58]. The zero-field phase difference of the electrons is different for each ring, and thus the interference disappears in the average (see also Sec. 3.1.2). The $h/2e$-periodic oscillations have been found in thin-walled diffusive metallic cylinders and their properties agree very well with theory [59].
For carbon nanotubes, only very few experimental evidences are reported. First indications for the $h/2e$-oscillations in multiwall carbon nanotubes have been found by Bachtold *et al.* [45]. Fujiwara *et al.* report oscillations with a flux periodicity of $h/3e$ and attribute this to inter-shell coupling [60].
In contrast, bandstructure calculations for a ballistic singlewall nanotube in a parallel field predict a h/e-periodic dispersion of the nanotube subbands, including an opening and closing of a bandgap with the same period (see Sec. 2.5.1). Experimental evidence for this have been obtained by photoluminescence measurements on singlewall tubes in a pulsed magnetic field [61], and by Coulomb blockade measurements on suspended multiwall tubes [62].
For the case that the magnetic field direction is perpendicular to the tube axis, the situation is not clear from both the theoretical and the experimental side. To our knowledge, all calculations show that the bandstructure is not modified much for small fields, where the magnetic length $\ell_m = \sqrt{\hbar/eB}$ is larger than the tube diameter D. Extensive bandstructure calculations have been performed by Ando *et al.* in the framework of $\mathbf{k}\cdot\mathbf{p}$-perturbation theory [13]. Here, for $\ell_m < D$, flat electronic energy bands are predicted to form, which in turn approach the (flat) Landau levels of (2D) graphene in the limit of high fields. In addition, the electron density is predicted to be localized at two diametral points of the tube circumference, where the magnetic flux through the tube surface is maximal.
Calculations within the tight-binding approach have been performed by Saito *et al.* [63]. Here, the electronic energy bands also become less dispersive with increasing magnetic field. The main difference to the findings of Ando *et al.* is that the energy bands oscillate as a function of the magnetic field, rather than approaching the graphene Landau levels. Although the oscillation amplitude decreases, no explicit Landau levels are predicted to form, even at high fields.
From the experimental side, there have not been made many attempts to measure bandstructure properties at high transversal magnetic fields. Kanda *et al.* report indications of bandstructure fingerprints in the Coulomb blockade pattern [64], while Lee *et al.* report indications of a change of the density of states with increasing perpendicular field [65]. Thus, no conclusive observations could be achieved up to now.
The majority of the experiments, both for parallel and perpendicular magnetic fields, suffers from the following fact: the diameter D of the investigated carbon nanotubes

is too small in order to have at least one flux quantum $\Phi_0 = h/e$ in the tube's cross section area $D^2\pi/4$. Especially for single walled tubes, the required magnetic fields are of the order ∼1000 T, which is far above the capability of a standard laboratory system.
Thus, it is highly desirable to investigate nanotubes with a sufficiently large diameter, which allow to determine the dominant electronic transport regime, and hence the appropriate theoretical approaches. Similar to the analysis in the preceding chapter, especially the interplay between bandstructure and disorder is of particular interest.

7.2 Sample Characterization and Doping State

The samples used for the measurements in this section were prepared by the random dispersion method (see Sec. 4.2), similar to those discussed in the preceding chapter. The Aharonov-Bohm field period $\Delta B_{\mathrm{AB}} = (h/e)/(r^2\pi)$ depends inversely proportional on the squared tube radius r. The same holds for the magnetic length, in order to match the tube radius: $B_{\mathrm{Landau}} = \hbar/e\ell_m^2$. For this reason, two tubes with large cross-sections have been investigated: sample C has a diameter of 29 nm and a length of 1.6 μm, while sample D has a diameter of 36 nm and a length of also 1.6 μm. We observe that large diameter tubes (>25 nm) are generally shorter (<2 μm) than the ones with smaller diameters (up to 10 μm). In addition, inspection in the scanning electron microscope (SEM) yields an increased number of growth irregularities and defects for the large diameter tubes. Both features are probably intrinsic properties of the arc-discharge growth method and make it harder to find clean tubes of a sufficient length.

A SEM image of sample D is presented in Fig. 7.1. The tube is located on an Al backgate and contacted by three Au finger electrodes from above. Two-terminal conductance measurements have been carried out, using the two upper electrodes. In Fig. 7.1, also the conductance of sample D as a function of the gate voltage at several temperatures is presented. Note that the curves for 6.5 K, 300 K (He) and 300 K (air) are offset by $0.1\times G_0$, $0.2\times G_0$ and $0.3\times G_0$, respectively, where $G_0 = 2e^2/h$. For all measurements, a low-frequency (f=37 Hz) ac bias voltage V with $eV_{\mathrm{rms}} < k_{\mathrm{B}}T$ has been applied, and the resulting ac current has been recorded. The uppermost trace shows the conductance G at 300 K in air at room pressure. The decrease of G with increasing gate voltage indicates a strong p-doping of the tube, in accordance with our former measurements. The second curve at 300 K shows the conductance after evacuation and application of a He atmosphere (∼200 mbar). Note that the

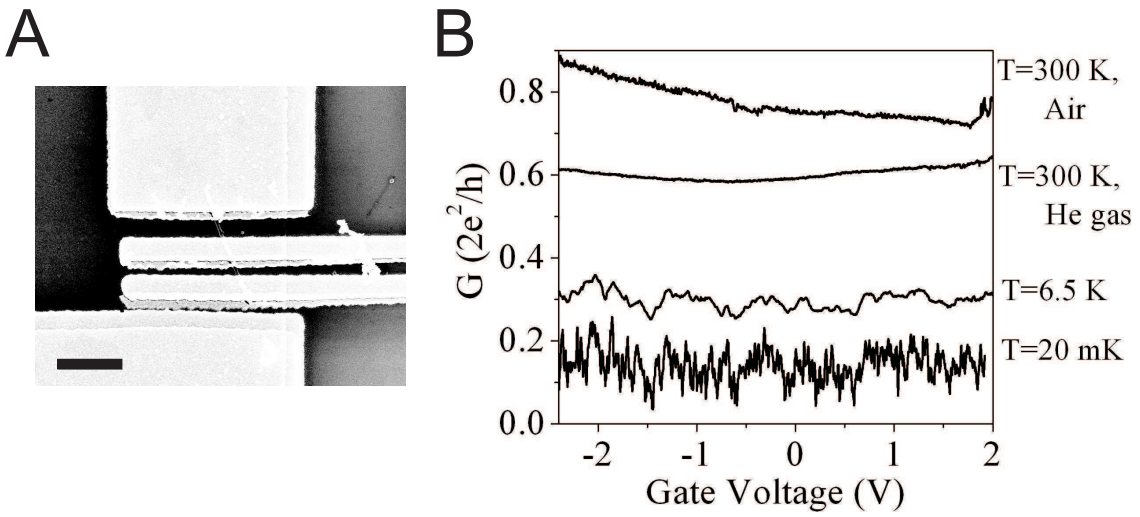

Figure 7.1: (A) Scanning electron micrograph of sample D. The tube is located on top of an Al gate and contacted by 3 Au finger electrodes. Only the two upper ones are used for the measurement. The scalebar is 1 μm. (B) Conductance vs. gate voltage for sample D at 300 K (in air and in He atmosphere), 6.5 K and 20 mK (top to bottom). Curves are offset for clarity.

same behavior is displayed in vacuum (not shown). Here the doping has decreased and changed from p to n. The trace shows a minimum, which can be assigned to the charge neutrality point, as in the preceding chapter. Monitoring the conductance during the evacuation procedure shows a gradual change of the doping on a timescale of $\sim$5 min (not shown). These observations lead us to the hypothesis that adsorbates on the tube may create a strong p-doping. These adsorbates are removed by the evacuation and a weak n-doping remains.

At lower temperatures, conductance oscillations arise, which are again attributed to an interplay of the bandstructure, one-particle quantum interference and two-particle Coulomb interaction effects. The trace at 20 mK shows that the conductance is not suppressed to zero at any gate voltage. This means that the sample does not enter the regime of dominating Coulomb blockade, down to the base temperature of the refrigerator. Instead, the conductance has a minimum in the vicinity of the charge neutrality point even at low temperatures, although large conductance fluctuations are present. This behavior is shown by both samples. It seems to occur preferably for nanotubes with large diameter, while thinner tubes enter the Coulomb blockade regime at temperatures of $\sim$200 mK. An enlarged lead capacitance could originate from the larger tube diameter, which reduces the charging energy of the tube. Thus, the Coulomb blockade regime may only be accessed at a temperature way below the base temperature of the system.

7.3 Conductance Oscillations in a Parallel Field

When a magnetic field is applied parallel to the axis of a nanotube, the conduction electrons can gain an Aharonov-Bohm phase only by moving around the tube circumference. In both the bandstructure and the quantum interference descriptions of transport, this leads to periodic oscillations in the magnetoconductance (see. Chapters 2, 3). Hence, for a first check, a single magnetoconductance trace has been

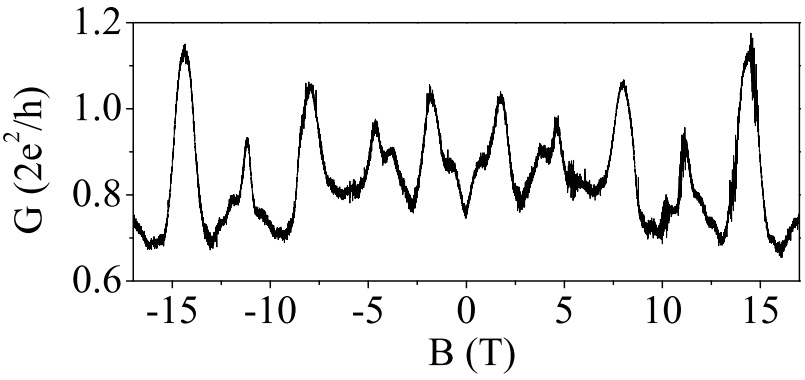

Figure 7.2: Differential conductance of sample C as a function of the magnetic field parallel to the tube axis. The temperature was 5 K.

recorded at zero gate voltage at a temperature of 5 K for sample C. The result for magnetic fields up to ±17 T is presented in Fig. 7.2. The trace is symmetric with respect to magnetic field reversal, as expected for a two-terminal configuration. The conductance shows a minimum at zero field, as well as an oscillation with a period ΔB of ∼3.2 T. Starting from $B = 0$, the conductance maxima at $\pm 0.5\Delta B$, $\pm 2.5\Delta B$ and $\pm 4.5\Delta B$ display an enhanced amplitude, while the amplitude at $\pm 1.5\Delta B$ and $\pm 3.5\Delta B$ is smaller.

For the measured tube diameter D of 29 ±1 nm, a flux of $h/2e$ through the tube cross section area $D^2\pi/4$ corresponds to ΔB=3.1 T. Thus, the periodicity ΔB agrees well with multiples of a flux of $h/2e$. The regular alternation of enhanced and reduced conductance peaks indicates that, in addition, h/e-periodic features are present.

At this stage, the origin of the oscillations cannot be determined: on one hand, $h/2e$ is the periodicity of the Altshuler-Aronov-Spivak oscillations, and thus suggests the dominance of quantum interference.

For a detailled insight in the flux periodicity of the conductance, magnetoconductance traces have to be taken for different values of the Fermi energy. Therefore, the linear response conductance has been recorded as a function of the gate voltage and the magnetic field. Similar to the procedure of sec. 6.3, the field was changed

in steps, while the gate voltage was swept continuously. The result for sample C is shown in Fig. 7.3, at temperatures of 1 K, 4.5 K and 20 K. The conductance G shows

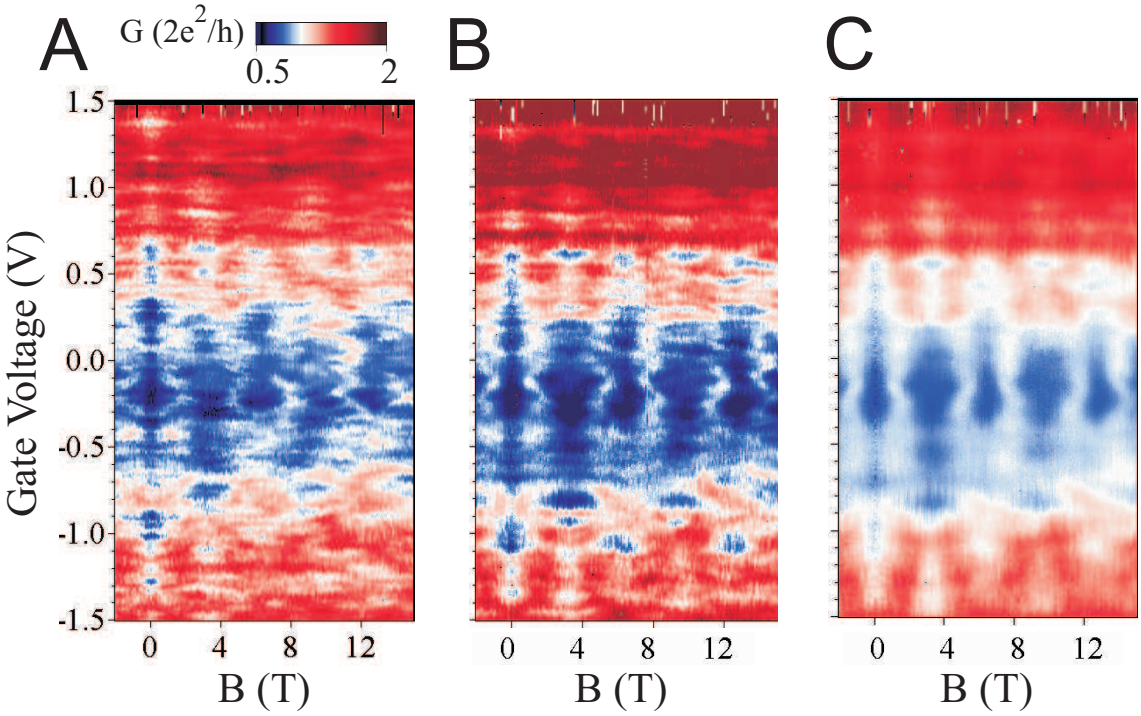

Figure 7.3: Color coded differential conductance of sample C as a function of the gate voltage and a magnetic field parallel to the tube axis at temperatures 1 K (A), 4.5 K (B) and 20 K (C). Red regions correspond to high conductance, while blue regions indicate low conductance.

a rich variety of structures. For each value of the magnetic field, G is minimal in the vicinity of $U_{\text{gate}} \sim -0.2$ V, which coincides with the position of the charge neutrality point (CNP), cf. Fig. 7.1. When the Fermi energy is tuned away from the CNP, the overall conductance increases. Around zero magnetic field, G has a minimum for most values of U_{gate}. In contrast to the measurements in a perpendicular field, additional minima arise with a field periodicity of ~ 3.1 T, which could be identified with multiples of a flux of $h/2e$ in the previous section. Additionally, conductance features with the double flux period, h/e, occur. The most intriguing observation is the presence of rhomb-shaped regions of high conductance, in the vicinity of the CNP. These features become smoother as the temperature is increased. Even at a temperature of 20 K, Fig. 7.3C, the two periodicities are still prominent, although the finest conductance fluctuations are washed out.

Figure 7.4 shows the result of the corresponding measurement for sample D at a temperature of 4.5 K. In order to elucidate the structure and the amplitude of the conductance oscillations, the data are also shown in a surface representation. The charge neutrality point is located at $U_{\text{gate}} = -0.6$ V, where a pronounced valley in

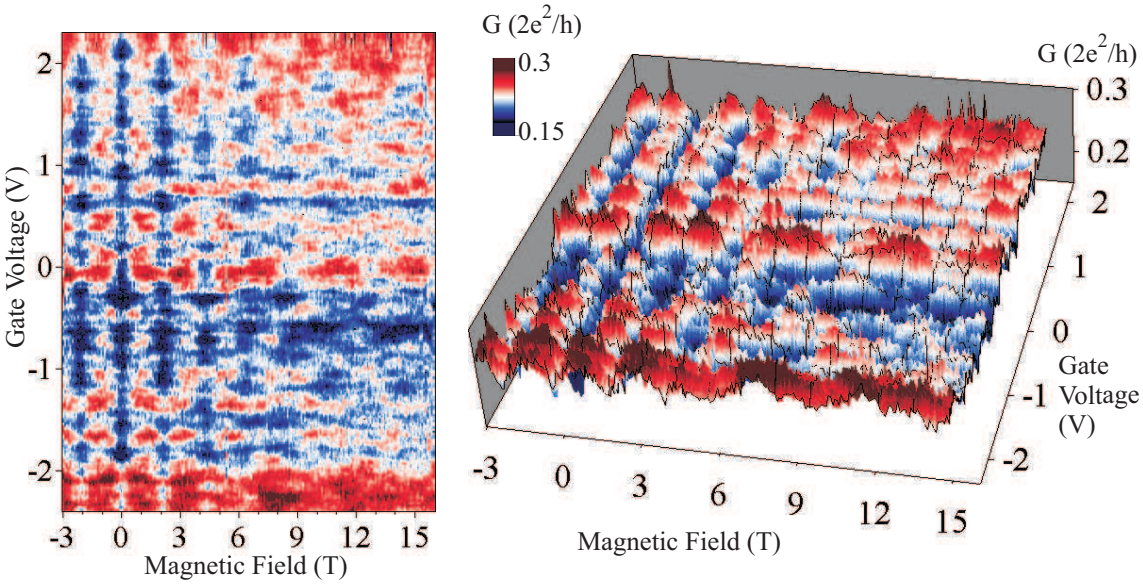

Figure 7.4: Left: Color coded differential conductance of sample D as a function of the gate voltage and a magnetic field parallel to the tube axis at 4.5 K. Red regions correspond to high conductance, while blue regions indicate low conductance. Right: Same data, but in a colored surface representation.

$G(U_{\text{gate}}, B)$ is located. Again, two specific field periodicities are identified, namely $\Delta B = 2.1$ T and $2\Delta B$. Also here, ΔB is in good agreement with a flux of $h/2e$: For the measured tube radius of 36 nm ±1 nm, the latter corresponds to 2.0 T ±0.3 T. The surface plot shows that the oscillations are present up to the highest magnetic fields, while their amplitude decreases. Note that the range of the gate voltage for sample D is more than twice as large as for sample C. Thus the 'frequency' of the conductance variations with gate voltage appears to be much higher than it actually is.

Based on these measurements, we would like to clarify, whether the data allow a decomposition into bandstructure- and interference contributions. Similar to the preceding chapter, it would be desirable to elucidate the modification of the quantum interference by the band structure and vice versa.

7.4 Field Dependence of the Magnetic Bandstructure

Bandstructure considerations have been applied successfully to the magnetoconductance, when the field is oriented perpendicular to the tube axis (see Chap. 6). Thus, similar approaches for the parallel field seem rewarding. In this case, one conceptual

difficulty arises from the fact that even small fields have a large effect on the density of states. Already the tight binding calculation shows that the van Hove singularities are splitted and shifted linearly in energy with increasing magnetic field. This results in a periodic magnetic dispersion, with a periodicity given by the Aharonov-Bohm flux h/e (see Sec. 2.5.1).

In accordance with most works in literature, the previous chapter has revealed that

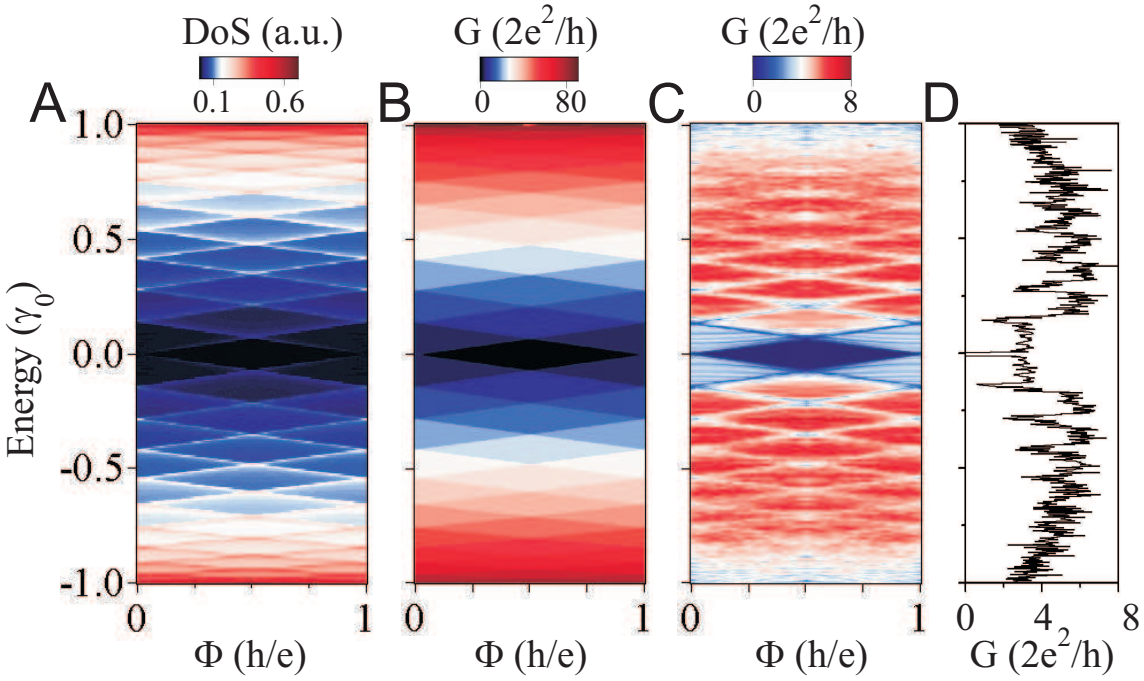

Figure 7.5: (A) Color representation of the calculated density of states for a (22, 22)-singlewall nanotube without disorder as a function of energy (in units of $\gamma_0 \sim 3$ eV) and a magnetic flux parallel to the tube axis. (B) Corresponding ballistic conductance. (C) Color representation of the conductance of the same tube as in A) and B), but with Anderson disorder of strength $W = \gamma_0/5$. (D) Zero-field conductance of the disordered tube as a function of energy.

multiwall carbon nanotubes appear to be strongly diffusive systems. Therefore, it is highly desirable to have theoretical estimates for the conductance of a disordered tube in a parallel magnetic field. This represents the basis for a qualitative and quantitative analysis of the measurements.

Such calculations have been performed by S. Roche and F. Triozon, using a recursive Green's function approach for the tight binding bandstructure [7]. This framework allows the inclusion of static on-site Anderson disorder (see Refs. [66, 67] and references therein).

The result of the calculation for a (22, 22) nanotube with a diameter of 3 nm is presented in Fig. 7.5. Fig. 7.5A shows a color representation of the density of states (DoS) as a function of energy and the magnetic flux through the tube. In

this case, the disorder is set to zero and lines of high density of states appear, in accordance with the simple bandstructure calculations in Sec. 2.5.1. These lines can be assigned to the (field dependent) positions of the subband onsets. They enclose diamond-shaped regions of constant conductance, as can be seen from Fig. 7.5B. There, a calculation of the corresponding (ballistic) conductance is presented.
This graph has to be compared now to Fig. 7.5C, which shows the conductance in the presence of on-site Anderson disorder of strength $W \in [-\gamma_0/5, \gamma_0/5]$. The disorder does not scramble the conductance pattern completely. The diamond-shaped regions are still visible, while the conductance at the diamond edges is suppressed to about half of the value on the plateau. Furthermore, the conductance does not anymore increase in steps as in the ballistic case, but even decreases slightly with the number of occupied channels. For illustration, a single conductance trace at zero field is shown in Fig. 7.5D. This behavior can be understood qualitatively by the behavior of the elastic mean free path L_{elastic}, as discussed in Sec. 6.7: both the numerical calculations and the experimental data indicate a strong decrease of L_{elastic} at the subband edges. This compensates the rise of the conductance due to the opening of new conduction channels.
In summary, the calculated conductance of a moderately disordered tube still reveals structural similarity to its DoS without disorder. Hence, it seems legitimate to compare calculations for the DoS directly to the measured data. This is especially important for large tube diameters: here in presence of disorder, the computational cost for the conductance calculation becomes quickly prohibitive with increasing tube diameter. In contrast, the clean DoS can be investigated up to large diameters.

7.5 Density of States vs. Measured Conductance

In order to find 'fingerprints' of the nanotube's bandstructure in the magnetoconductance patterns, the calculated density of states (DoS) is compared to the measured conductance. The procedure is to a large extent identical to the one performed for the perpendicular field case, cf. Sec. 6.4.

The major problem is to convert the energy axis E of the DoS, $\nu(E)$, into an equivalent (nonlinear) gate voltage scale U_{gate}, in order to extract $\nu(U_{\mathrm{gate}})$. In turn, $\nu(U_{\mathrm{gate}})$ gives information on the gate voltages, which are necessary in order to populate given nanotube subbands. This is done (again) by assuming a constant capacitance C_{gate} between the tube and the gate electrode. Then the number of excess electrons $n(E_{\mathrm{F}})$ at a given Fermi energy E_{F} (with respect to the charge neu-

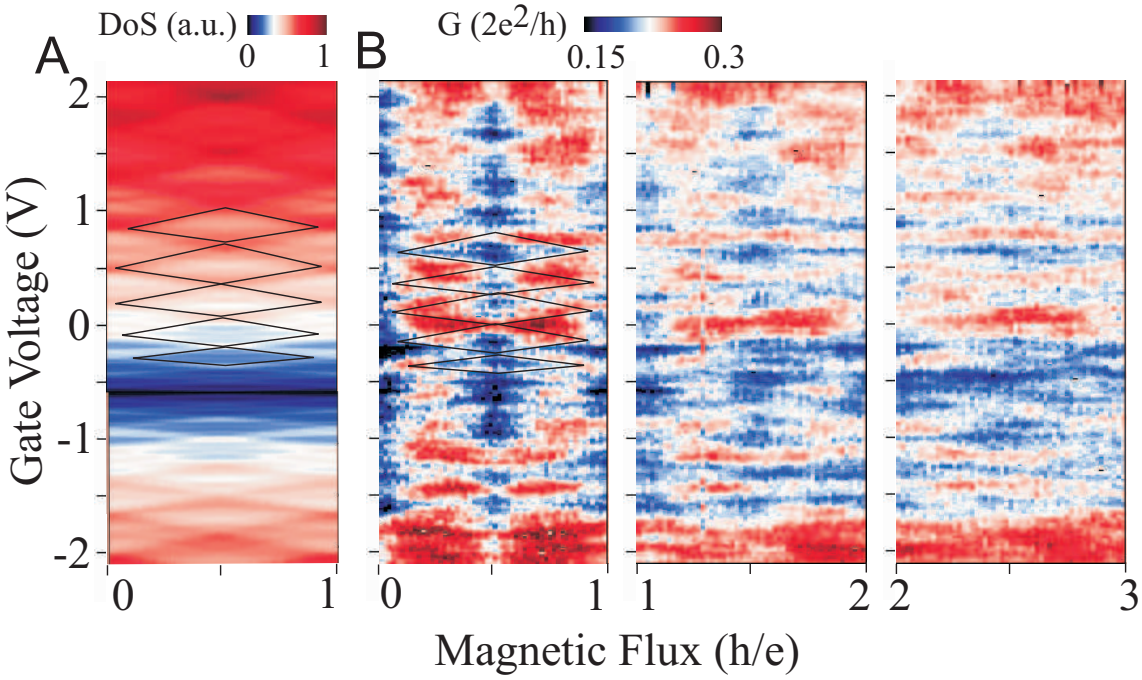

Figure 7.6: (A) Color representation of the calculated density of states (DoS) for a (260,260)-singlewall nanotube without disorder as a function of gate voltage and a magnetic flux parallel to the tube axis. Some diamond-shaped lines of high DoS are indicated. (B) Color representation of the measured conductance of sample D at 4.5 K for a magnetic flux from 0 to Φ_0 (left), Φ_0 to $2\Phi_0$ (middle) and $2\Phi_0$ to $3\Phi_0$ (right), where $\Phi_0 = h/e$. Diamond-shaped lines of enhanced conductance are marked.

trality point) is connected to the gate voltage U_{gate} by

$$U_{\text{gate}}(E_{\text{F}}) = \frac{e}{C_{\text{gate}}} n(E_{\text{F}}), \tag{7.1}$$

where $n(E_{\text{F}})$ is given by the integral over the DoS,

$$n(E_{\text{F}}) = L \int_0^{E_{\text{F}}} \nu(E) \mathrm{d}E. \tag{7.2}$$

Here, L is the length of the nanotube. Hence, plotting $\nu(E_{\text{F}})$ vs. $U_{\text{gate}}(E_{\text{F}})$ gives the desired result. The procedure has been performed for the calculated DoS of a (260, 260) nanotube and for a magnetic flux from 0 to h/e.

For a quantitative comparison with the measurement, the knowlegde of the coupling capacitance C_{gate} is crucial. In Sec. 6.4, C_{gate} was obtained from an explicit assignment of the subband onsets to certain gate voltages. Unfortunately, this procedure does not work for large diameter tubes, mainly due to the complexity of the magnetoconductance for both parallel and perpendicular fields[1]. Therefore, a typical

[1]The magnetoconductance of sample C in a perpendicular field will be discussed in Sec. 7.7

capacitance of 300 aF/μm has been used. Since both samples in Sec. 6.4 rendered a capacitance of this magnitude, we take it as an approximation also in the present case.

The result is presented in Fig. 7.6 as a color representation, together with the magnetoconductance measurement for sample D at 4.5 K. The magnetic field scale has been converted into a flux scale in units of h/e. In order to highlight h/e-periodicities, the data have been split up into three segments. The rescaled calculation shows diamond-shaped lines of high DoS, which are superposed on an increasing background, identical to Fig. 7.5. Due to the rescaling, the diamonds are distorted as a function of gate voltage. Some diamonds close to the charge neutrality point (CNP) are marked with lines. The CNP is located at the experiental value of -600 mV.

A closer look at the data reveals, that also here diamond-shaped lines of high conductance can be identified. As a guide to the eye, some of them have been marked by lines.

Although these similarities are not sufficient for a one-to-one assignment of calculation and experiment, they nevertheless demonstrate that the position, the shape and also the size of the diamonds agree well. Therefore, the value of the capacitance seems roughly correct, as well as the bandstructure model. Furthermore, the assignment is supported by the following fact: in the case, where an exact assignment of van-Hove singularities and quenched magnetoconductance was possible (Sec. 6.4), the peaks in the DoS also appeared to correspond to small peaks in the conductance, rather than to conductance steps expected in ballistic conductors.

At higher multiples of h/e, the data show indeed a repetition of the conductance pattern, although with a smaller amplitude. This can also be taken for an argument for the presence of bandstructure effects, since weak localization-like quantum interference alone would just give a $h/2e$-modulation.

In conclusion, the nanotube's bandstructure seems to strongly affect its conductance also in the case of a parallel magnetic field. Due to the strong variation of the DoS with the magnetic flux, the effects here are even more pronounced than in the perpendicular case and for smaller tube diameters. An exact assigment of calculated van-Hove singularities and experimental magnetoconductance peaks is not possible. Nevertheless, the strong similarity with the measured conductance patterns reveals first clear signatures of the specific nanotube bandstructure effects in the magnetoconductance.

7.6 Contribution of Quantum Interference

The $h/2e$-periodic modulation of the magnetoconductance in Fig. 7.4 gives rise to the question, to which extent coherent backscattering is involved into the transport properties, similar to the discussion of Sec. 6.5 for the perpendicular field.

Much insight can be gained by averaging over magnetoconductance traces for many

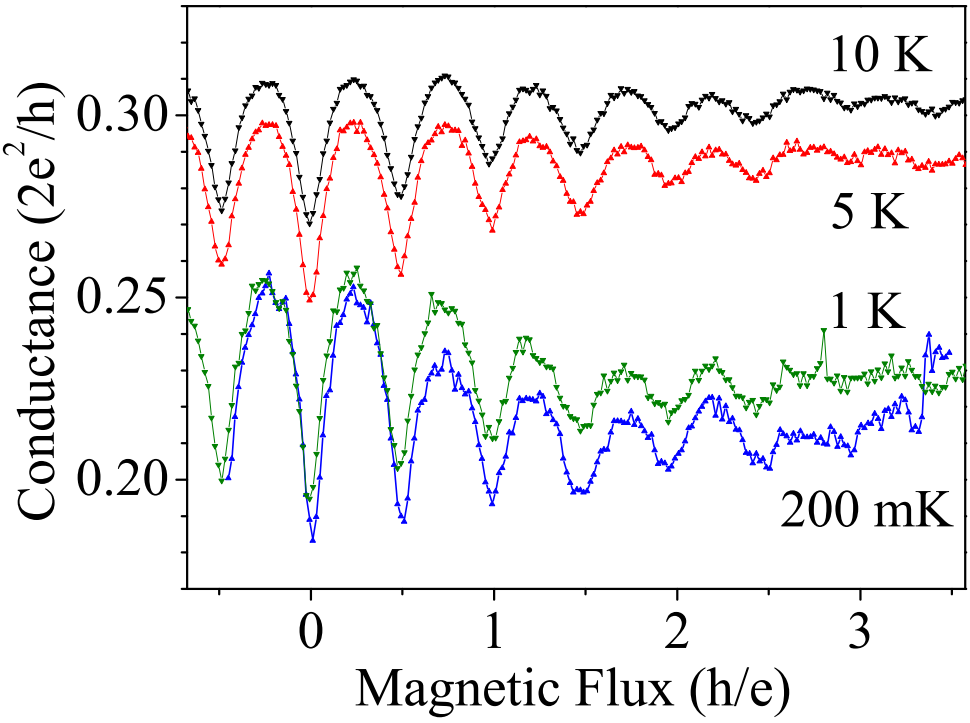

Figure 7.7: Magnetoconductance of sample D (triangles) averaged over the interval [−2.3 V, 2.3 V] of gate voltage at temperatures 10 K, 5 K, 1 K and 200 mK (top to bottom).

gate voltages. Bandstructure effects are expected to be smoothed by the average, as well as universal conductance fluctuations. Thus, averages over the whole gate bandwidth has been done for both samples. The result for sample D is presented in Fig. 7.7. For all temperatures, the averages show a strong $h/2e$-periodic modulation. The amplitude of the oscillation decreases both with increasing temperature and increasing magnetic flux. Especially at small fields, the oscillations are anharmonic, i.e. sharp dips appear, while the peaks are smoother.

All these curves bear a strong similarity to Altshuler-Aronov-Spivak (AAS) oscillations in diffusive metallic cylinders [59]. The theory predicts an anharmonicity of the

magnetoconductance oscillations. It is explained in terms of time-reversed, diffusive and phase coherent electron paths, which revolve the cylinder circumference more than one time. Thus, several multiples of the 'AAS-flux' $h/2e$ are enclosed, which in turn leads to higher harmonics in the Fourier expansion of the magnetoconductance trace.

In analogy to the weak-localization fits for the averaged magnetoconductance traces in a perpendicular field (see 6.5), the averaged trace at 10 K has been fitted with AAS oscillations, cf. Eq. 3.8. The fitting was done in the range $[-2h/e, 2h/e]$, with two free parameters, namely the phase coherence length L_φ and the angle Θ between the tube axis and the magnetic field, cf. Eq. 3.10. The result is presented in Fig. 7.11. The best fit was achieved for L_φ=30 nm and $\Theta = 2$ degrees. These

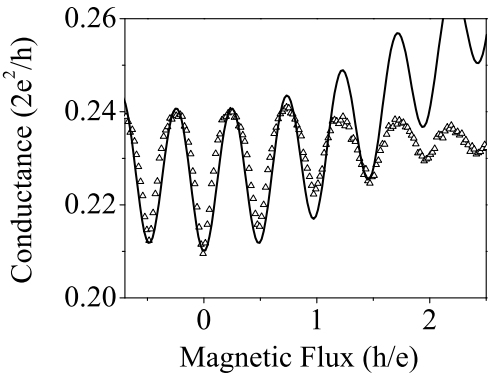

Figure 7.8: Averaged magnetoconductance at 10 K (open triangles). The line is a fit of AAS-oscillations to the data.

parameters are reasonable for the temperature of 10 K (L_φ) and the experimental accuracy for the alignment of the tube with respect to the field (Θ).

Note that the fitting procedure is not capable of delivering an estimate for the actual wall thickness in which the transport takes place, or, in other words, the number of current carrying nanotube shells. The reason is revealed in the equation for the effective wall thickness, Eq. 3.10. There, even a small misalignment Θ of tube and field leads to an effective width a^* of several nanometers, which is much larger than the intershell distance of ~ 0.3 nm. Thus, a^* is predominantly determined by Θ.

Recent experiments by Bourlon *et al.* revealed that for multiwall nanotubes the intershell conductance is of the same order as the longitudinal conductance of a single shell [6]. Our experimental data do not allow the extraction of any explicit number of nanotube shells, which carry the current. Nevertheless, a coarse indication is given by the oscillation period ΔB of the AAS-like conductance oscillations. ΔB reflects the average shell diameter, where transport takes place. Since this diameter matches very well the measured tube radius, it is very likely that only the outermost

shell is involved, together with few neighboring shells.
Within the fitting range, the accordance of data and fit is fairly good. For higher fields, large deviations occur. The fitted curve shows a rising background originating from weak localization in a slightly misaligned field: here also a significant number of time-reversed trajectories contribute, which do not enclose the cylinder axis. The rising background is an intrinsic property of the AAS-oscillations, which is obviously not met by the measurement. Additionally, the oscillation amplitude of the theoretical curve decays much slower at higher fields.

At this point, two questions arise. Firstly, one can doubt, whether the origin of

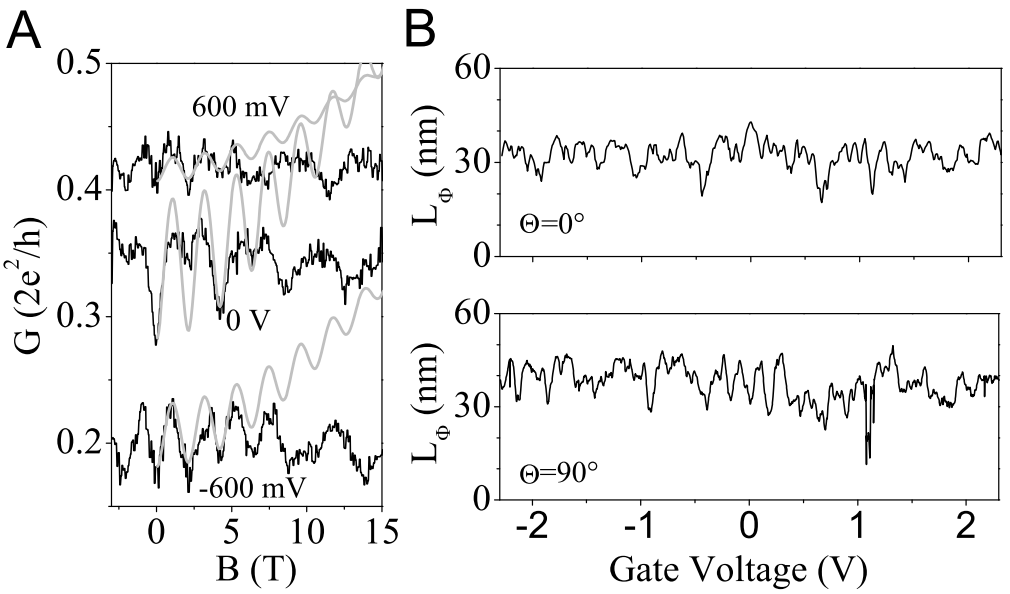

Figure 7.9: (A) Black lines: representative magnetoconductance traces at gate voltages U_{gate}= 0.6 V, 0 V and -0.6 V (top to bottom). Grey lines represent fits of AAS theory. (B) Phase coherence length vs. gate voltage for sample D at 4.5 K. For parallel (top) and perpendicular fields (bottom), AAS-theory and quasi-1D WL-theory is applied, respectively.

the oscillations is indeed AAS-type quantum interference, since the overall quality of the fit is not very good. Secondly, it is not clear, if an averaged conductance trace conceptually allows a fit by a single AAS-type curve. With respect to the second question, consider a set of AAS-type conductance traces with different phase coherence lengths. Then, the average trace cannot be expressed in terms of a single AAS-trace with an average phase coherence length.
Both questions can be overcome by the following approach. Like in Sec. 6.5, the phase coherence length has to be determined for each value of the gate voltage sep-

arately. This, in turn has to be performed for a magnetic field both parallel and perpendicular to the tube axis. For the perpendicular case, 'conventional' 1D weak localization theory is applied , while AAS-oscillations are fitted in the parallel case. For a given gate voltage U_{gate}, the phase coherence length $L_\varphi(U_{\mathrm{gate}})$ in zero magnetic field should not depend on the tube orientation. Since the weak localization approach is nearly established for perpendicular fields, both fitting procedures are supposed to give the same value , if the AAS-description is correct. In addition, by this procedure also the problem of interpreting an averaged trace is avoided.
The corresponding magnetoconductance measurement in a perpendicular field has also been performed for samples C and D. The result will be shown and discussed in Sec. 7.7. For small fields, the data allow fitting of 1D weak localization theory. For the measurement in a parallel field, AAS theory has been fitted in a range $[-2h/e, 2h/e]$, where there is a good accordance of theory and experiment. The result is presented in Fig. 7.9. Three representative magnetoconductance traces are also presented, together with the corresponding fitted AAS-traces. It turns out that the extracted phase coherence lengths agree very well within the accuracy of the fitting procedure, which is of the order 5–10 nm. Both traces show the same qualitative behavior, i.e. the occurence of peaks and dips. The same holds for the absolute values for L_φ, which vary between 20 nm and 40 nm. This result confirms that the $h/2e$-periodic oscillations are indeed explained by the AAS theory.
Note that all observed phase coherence lengths are much smaller than the tube circumference, which amounts ∼110 nm. Thus, the samples are already in the regime, for which the AAS oscillations are predicted to be damped exponentially. Therefore, experiments with tubes with less defects are very likely to produce more pronounced AAS-oscillations.
In summary, the partial interpretation of the experimental results in terms of quantum interference appears to be justified also for parallel magnetic fields. The periodicity of the oscillations favors diffusive electron transport through few outermost nanotube shells.

7.7 Conductance Variations in a Perpendicular Field

For multiwall carbon nanotubes with large diameters of the order ∼ 30 nm, bandstructure calculations predict some modulations of the bandstructure with perpendicular magnetic field, starting already at B ∼2 T. Such measurements are described in the following. The results are compared to numerical bandstructure calculations carried out by S. Roche and F. Triozon [7].

Magnetoconductance measurements in perpendicular fields up to 15 T have been carried out for sample C, which has a tube diameter of ~ 29 nm. The relevant field scale is given by the ratio of the tube radius R and the magnetic length $L_{\mathrm{m}} = \sqrt{\hbar/eB}$, which is referred to as the dimensionless magnetic field b:

$$b = \frac{R^2}{L_{\mathrm{m}}^2} = R^2 \frac{eB}{\hbar}. \tag{7.3}$$

For the given tube diameter, b=1 corresponds to $B = 1.7$ T, while for the maximum field of 16 T, b=3.

In order to have a quantitative theoretical prediction, numerical bandstructure

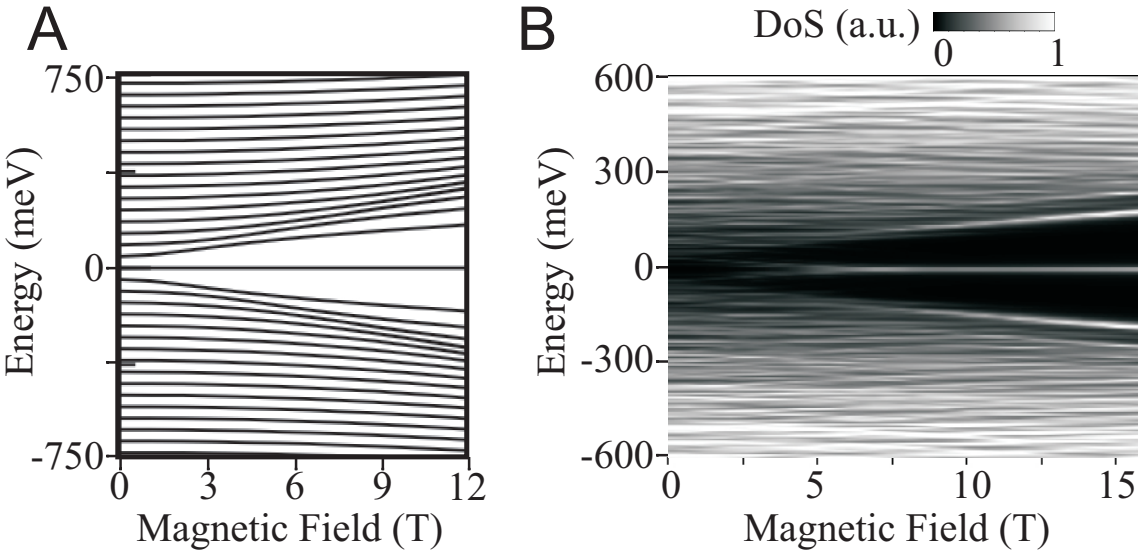

Figure 7.10: (A) Tight-binding bandstructure calculation for a (210, 210) armchair nanotube: Energy levels at the K-point as a function of a magnetic field perpendicular to the tube axis. (B) Greyscale representation of the calculated density of states vs. magnetic field at smaller energies (Figure adapted from [7]).

calculations for ballistic (210,210)-nanotubes have been performed, using the tight-binding approach [7]. The result is presented in Fig. 7.10. Fig. 7.10A shows the evolution of the energy levels at the K-point with increasing perpendicular field. A shift of the energy levels towards higher energies occurs. Note that the states at the K-point denote the bottoms of the one-dimensional subbands in zero magnetic field. Thus, Fig. 7.10A provides a guideline for the shift of all levels. Starting from zero field, the energy shift is becoming significant as soon as the dimensionless magnetic field b approaches unity, i.e. already below 2 T.

The corresponding density of states is presented in Fig. 7.10B. Its shape is partially anticipated by the K-point dispersion. For fields above 5 T, the regions of high density of states are also shifted towards higher energies. At the same time, a state

of high density of states forms around zero energy. This regions resembles a Landau level at zero energy. Nevertheless, the tight binding approach does not predict an explicit Landau level formation, cf. Sec. 7.1.

The conductance of sample C has been measured as a function of gate voltage and perpendicular magnetic field. The result for T=1K is presented in Fig. 7.11A in a color representation. The graph bears some similarities with the analogous measurement for thinner tubes, cf. Sec. 6.3. The conductance is reduced at $B = 0$ for all values of the gate voltage. This is again attributed to weak localization, that should be the dominating contribution to magnetotransport fingerprints especially at low fields. Conversely to the parallel case, no effects of the bandstructure at low fields are expected. For magnetic fields above 2 T, a strong shift of regions of high conductance towards higher gate voltages with magnetic field is observed. The shifting appears to be much more significant for the region of positive gate voltages, than for the negative region. Note that such a shift is not observed for the thinner tubes in a perpendicular field (see the preceding chapter).

For comparison, in Fig. 7.11B the calculated density of states has been rescaled with the gate voltage. The procedure is the same as in Sec. 7.5, and again an average gate capacitance of 300 aF/μm is used. Again, the result represents a distorted reproduction of the DoS (see Fig. 7.10B). The corresponding nonlinear energy scale is also presented in Fig. 7.11B. Thus, a range of 3 V for the gate voltage yields a shift of the Fermi energy of about 400 meV.

The preceding chapters revealed strong similarities of the regions of high conductance in the experiment to those with high density of states in the calculation. In particular, at positive gate voltages the experimental 'bands' of high conductance are shifted towards higher voltages, as the field is increased. Also, several regions of high conductance appear to be shifted towards the charge neutrality point (CNP, located at $U_{\mathrm{gate}} = -200$ mV), as the magnetic field is increased. On the other hand, several features do not match. Most prominent is the asymmetry of the experimental conductance pattern: the 'bands' for negative gate voltages rather move towards the CNP than to more negative values. In addition, several regions of high density of states coincide with regions of conductance minima.

In conclusion, it is safe to say that the results of experiment and calculation at least point into the same direction. The numerical simulation can qualitatively explain the strong magnetic field dispersion of the conductance. Like in the case of the parallel magnetic field, an exact assignment of conductance peaks to van-Hove singularities in the density of states is not possible within our experimental scope. This may be related to the smaller subband spacing of the thicker tubes.

The measurement demonstrates that the magnetic dispersion of large diameter nanotubes in a perpendicular field is now experimentally accessible. Thus, systematic

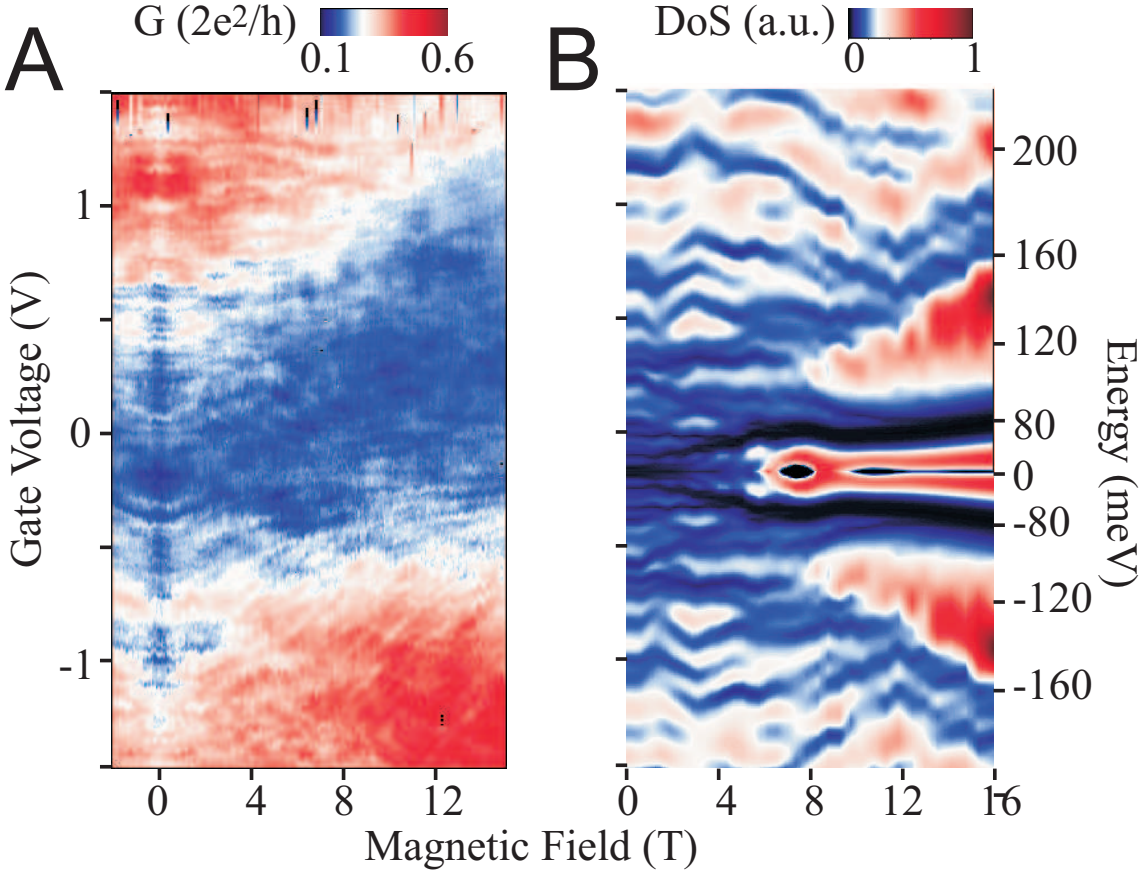

Figure 7.11: (A) Color representation of the conductance of sample C as a function of gate voltage and perpendicular magnetic field at 1 K. (B) Numerical calculation of the density of states as a function of gate voltage and perpendicular magnetic field. Therefore, the energy scale of the DoS has been converted into a gate voltage by the use of a gate capacitance of C_{gate} =300 aF. The energy scale is attached on the right.

future experiments are necessary to clarify the situation.

7.8 Discussion

In this chapter, measurements for large diameter multiwall carbon nanotubes in high parallel and perpendicular fields have been reported. The results have been compared to existing theoretical approaches, namely the Altshuler-Aronov-Spivak theory for quantum interference and tight-binding calculations for the bandstructure. It turned out that for a successful explanation of the results, both bandstructure and quantum interference effects have to be jointly taken into account, since each approach only partly covers the observed magneto-fingerprints.

Now the question arises, if the interference properties are modified by the bandstructure and vice versa, like the quench of the weak localization at subband onsets for the small diameter tubes, see Sec. 6.5. Here, this is much more difficult to detect. The main reason is the fast change of both the predicted band dispersion and the observed conductance with magnetic field.
At least, the overall shape of the conductance traces finds itself in accordance with the ones from Sec. 6.3. Especially, the conductance shows a relatively weak overall modulation, with small peaks at the tentative subband onsets. The latter can be identified to some extent by the rhomb-shaped conductance features for a parallel field. This observation again favors a sharp drop of the elastic mean free path L_{el} at the subband onsets, which in turn leads to a compensation of the increased density of states in the conductance, cf. Sec. 6.7.
Thus, we are left with the insight that there is still a lot of work to do in order to understand the conductance properties of multiwall nanotubes at low temperatures. In order to elucidate these features more clearly, experiments with less diffusive tubes would be highly desirable, since there the bandstructure effects are expected to become more prominent.

Chapter 8

Summary and Outlook

This thesis has been focused on electronic transport properties of multiwall carbon nanotubes.
To study those properties experimentally, single nanotubes have been placed on an oxidized Al backgate electrode, which provides a strong electrostatic coupling. As source and drain, Au electrodes with low contact resistance have been attached afterwards.
The differential conductance of the nanotubes was measured at low temperatures, as a function of the magnetic field, the dc bias voltage, and the position of the Fermi energy. The latter was shifted over a large energy range by means of the gate voltage.
Already the preliminary measurements, as presented in Chap. 5, indicate the presence of strong disorder in the nanotubes. The successful interpretation of the data in terms of quantum interference effects like universal conductance fluctations and weak localization allows an estimation of mesoscopic lengthscales in the sample, such as the phase coherence length L_φ. One important observation is that the weak localization contribution to the conductance, and hence L_φ varies strongly with the position of the Fermi energy.
This fact served as the main motivation for more extensive and systematic magnetoconductance measurements, as descibed in Chap. 6. By these measurements, the values for the gate voltage, which are necessary to populate the nanotube's subbands, could be identified. These positions match well with the positions of the van Hove singularities in the density of states, as estimated from simple bandstructure models.
From the experimental magnetoconductance traces, L_φ was derived as a function of the Fermi energy. $L_\varphi(E_\mathrm{F})$ was found to be strongly reduced at the subband onsets, which corresponds to a quench of weak localization. There, also the elastic mean

free path L_{el} turned out to decrease steeply, in accordance with recent numerical calculations. Thus, a strong increase of the diffusivity of the system at the subband onsets was observed. This in turn allows the statement that a strong interplay between the bandstructure and the diffusion properties of multiwall nanotubes is present.

In addition, the study of the nonlinear conductance revealed a suppression of the zero bias anomaly at the subband bottoms, which has been interpreted as a reduction of electron-electron interactions. A similar result is obtained by extracting the interaction strength from the elastic mean free path.

Magnetoconductance measurements for large diameter nanotubes in a magnetic field parallel to the tube axis have been presented in Chapter 7. The results confirm the impression of the preceding sections: for a comprehensive understanding of the conductance properties, both the bandstructure and quantum interference have to be taken into account. The former manifests itself in a characteristic magnetic band dispersion, whose flux periodicity of h/e originates from the Aharonov-Bohm phase of the electrons. The latter appears as a superposition of $h/2e$-periodic oscillations in the magnetoconductance, which are successfully explained in terms of coherent backscattering.

Our interpretation of the results is strongly supported by numerical tight-binding calculations for both the density of states and the conductance in presence of a magnetic field and Anderson disorder.

Finally, complementary measurements for the large diameter nanotubes in a perpendicular magnetic field have been performed. The results provide the consistency of the description of the conductance in terms of quantum interference. In addition, a strong dispersion of the conductance with magnetic field is observed. These features partially match the predictions of numerical calculations for nanotubes in large magnetic fields.

The measurements as presented in this thesis render some more insight into the conductance properties of multiwall nanotubes. Nevertheless, there is still a lot of work to be done. For example, experiments on less disordered tubes would be highly desirable in order to study the transition from the ballistic to the diffusive regime. In addition, a combination of tunneling spectroscopy experiments and conductance measurements would allow to have a direct measure of the (tunneling) density of states.

Bibliography

[1] J. Reichert, R. Ochs, D. Beckmann, H. B. Weber, M. Mayor, H. v. Löhneysen, Phys. Rev. Lett. **88**, 176804 (2002).

[2] S. Iijima, Nature **354**, 56 (1991).

[3] Ch. Schoenenberger, A. Bachtold, C. Strunk, J.-P. Salvetat, Appl. Phys. A **69**, 283 (1999).

[4] P. G. Collins, Ph. Avouris, Sci. A. page 38 (Dec. 2000).

[5] F. Kreupl, A. P. Graham, G. S. Duesberg, W. Steinhoegl, M. Liebau, E. Unger, W. Hoenlein, Microelectronic Engineering **64**, 399 (2002).

[6] B. Bourlon, C. Miko, L. Forró, D. C. Glattli, A. Bachtold, Phys. Rev. Lett. **93**, 176806 (2004).

[7] S. Roche and F. Triozon, Private Communication.

[8] Y. Aharonov, D. Bohm, Phys. Rev. **115**, 485 (1959).

[9] R. Saito, M. S. Dresselhaus, G. Dresselhaus: *Physical Properties of Carbon Nanotubes*, Imperial College Press, London, (1998).

[10] P. R. Wallace, Phys. Rev. **71**(9), 622 (1947).

[11] M. S. Dresselhaus, G. Dresselhaus, K. Sugihara, I. L. Spain, H. A. Goldberg: *Graphite Fibers and Filaments*, Band 5, Springer Verlag, Berlin, (1988).

[12] J. M. Luttinger, Phys. Rev. **84**, 814 (1951).

[13] H. Ajiki, T. Ando, J. Phys. Soc. Jap. **62**, 1255 (1993).

[14] C. W. J. Beenakker, H. van Houten: *Quantum Transport in Semiconductor Nanostructures*, in H. Ehrenreich, D. Turnbull (Hrsg.): Solid State Physics: Advances in Research and Application, Band 44, Academic Press, (1991).

[15] P. W. Anderson, E. Abrahams, T. V. Ramakrishnan, Phys. Rev. Lett. **43**, 718 (1979).

[16] L. P. Gorkov, A. I. Larkin, D. E. Khmel'nitskii, JETP Lett. **30**, 228 (1979).

[17] R. P. Feynman, A. R. Hibbs: *Quantum Mechanics and Path Integrals*, McGraw-Hill, New York, (1965).

[18] B. L. Altshuler, A. G. Aronov, JETP Lett. **33**, 499 (1981).

[19] B. L. Altshuler, A. G. Aronov, B. Z. Spivak, JETP Lett. **33**, 94 (1981).

[20] B. L. Altshuler, JETP Lett. **41**, 648 (1985).

[21] P. A. Lee, A. D. Stone, Phys. Rev. Lett. **55**, 1622 (1985).

[22] B. L. Altshuler, D. E. Khmel'nitskii, JETP Lett. **42**, 359 (1985).

[23] C. W. J. Beenakker, H. van Houten, Phys. Rev. B **37**, 6544 (1988).

[24] L. P. Kouwenhoven, G. Schön, L. L. Sohn: *Introduction to mesoscopic electron transport*, in L. L. Sohn (Hrsg.): Mesoscopic electron transport, Band 345, NATO ASI series, (1997).

[25] H. Grabert, Z. Phys. B - Condensed Matter **85**, 319 (1991).

[26] B. L. Altshuler, A. G. Aronov, D. E. Khmel'nitskii, Solid State Comm. **39**, 619 (1981).

[27] T. Ando, T. Takeshi, J. Phys. Soc. Jap. **67**, 1704 (1998).

[28] C. T. White, T. N. Todorov, Nature **411**, 649 (1998).

[29] C. Kane, M. P. A. Fisher, Phys. Rev. B. **46**, 15233 (1992).

[30] M. Bockrath, D. H. Cobden, J. Lu, A. G. Rinzler, R. E. Smalley, L. Balents, P. L. McEuen, Nature **397**, 598 (1999).

[31] M. Krüger, I. Widmer andT. Nussbaumer, M. Buitelaar, C. Schönenberger, New J. Phys. **5**, 138 (2003).

[32] R. Egger, A. O. Gogolin, Phys. Rev. Lett. **87**, 066401 (2001).

[33] R. Tarkiainen, M. Ahlskog, J. Penttilä, L. Roschier, P. Hakonen, M. Paalanen, E. Sonin, Phys. Rev. B **64**, 195412 (2001).

[34] A. Kanda, K. Tsukagoshi, Y. Aoyagi, Y. Ootuka, Phys. Rev. Lett. **92**, 036801 (2004).

[35] J.-M. Bonard, T. Stora, J.-P. Salvetat, F. Maier, T. Stöckli, C. Duschl, L. Forró, W. A. de Heer, A. Châtelain, Adv. Mater. **9**, 827 (1997).

[36] S. H. M. Persson, L. Olofsson, L. Gunnarsson, Appl. Phys. Lett. **74**, 2546 (1999).

[37] A. Bachtold, P. Hadley, T. Nakanishi, C. Dekker, Science **294**, 1317 (2001).

[38] R. Krupke, F. Hennrich, H. B. Weber, D. Beckmann, O. Hampe, S. Malik, M. M. Kappes, H. v. Löhneysen, Appl. Phys. A **76**, 397 (2003).

[39] B. Stojetz, Ch. Hagen, Ch. Hendlmeier, E. Ljubovic, L. Forró, Ch. Strunk1, New J. Phys. **6**, 27 (2004).

[40] C. Dekker, Physics Today **52**, 22 (1999).

[41] S. Frank, P. Poncharal, Z. L. Wang, W. A. de Heer, Science **280**, 1744 (1998).

[42] A. Urbina, I. Echeverría, Z. L. Wang, A. Pérez-Garrido, A. Díaz-Sánchez, J. Abellán, Phys. Rev. Lett. **90**, 106603 (2003).

[43] L. Langer, V. Bayot, E. Grivei, J.-P. Issi, J. P. Heremans, C. H. Olk, L. Stockman, C. Van Haesendonck, Y. Bruynseraede, Phys. Rev. Lett. **76**, 479 (1996).

[44] K. Liu, Ph. Avouris, R. Martel, W. K. Hsu, Phys. Rev. B **63**, 161404 (2001).

[45] A. Bachtold, Ch. Strunk, J.P. Salvetat, J.M. Bonard, L. Forro, Th. Nussbaumer, Ch. Schönenberger, Nature **397**, 673 (1999).

[46] A. Bachtold, M. de Jonge, K. Grove-Rasmussen, P. L. McEuen, M. Buitelaar, C. Schönenberger, Phys. Rev. Lett. **87**, 166801 (2001).

[47] R. Saito, G. Dresselhaus, M. S. Dresselhaus, J. Appl. Phys. **73**, 494 (1993).

[48] S. Tans, R. M. Verschueren, C. Dekker, Nature **393**, 49 (1998).

[49] P. L. McEuen, M. Bockrath, D. H. Cobden, Y.-G. Yoon, S. G. Louie , Phys. Rev. Lett. **83**, 5098 (1999).

[50] M. R. Buitelaar, A. Bachtold, T. Nussbaumer, M. Iqbal, C. Schönenberger, Phys. Rev. Lett. **88**, 156801 (2002).

[51] J.-Y. Park, S. Rosenblatt, Y. Yaish, V. Sazonova, H. Üstünel, S. Braig, T. A. Arias, P. W. Brouwer, P. L. McEuen, Nano Lett. **4**, 517 (2004).

[52] A. Javey, J. Guo, M. Paulsson, Q. Wang, D. Mann, M. Lundstrom, H. Dai, Phys. Rev. Lett. **92**, 106804 (2004).

[53] F. Triozon, S. Roche, A. Rubio, D. Mayou, Phys. Rev. B **69**, 121410 (2004).

[54] M. J. Kearney, P. N. Butcher, J. Phys. C: Solid State Physics **21**, 2539 (1988).

[55] S. Hügle, R. Egger, Phys. Rev. B (66), 193311 (2002).

[56] H. T. Man, A. F. Morpurgo, cond-mat/04011141v1 (2004).

[57] Bouchiat, private communication (2004).

[58] R. B. Laibowitz, S. Washburn, R. A. Webb, C. P. Umbach, C. Van Haesendonck, Phys. Rev. Lett. **56**, 386 (1986).

[59] D. Yu Sharvin, Yu V. Sharvin, JETP Lett. **34**, 272 (1981).

[60] A. Fujiwara, K. Tomiyama, H. Suematsu, M. Yumura, K. Uchida, Phys. Rev. B **60**, 13492 (1999).

[61] S. Zaric, G. N. Ostojic, J. Kono, J. Shaver, V. C. Moore, M. S. Strano, R. H. Hauge, R. E. Smalley, X. Wei, Science **304**, 1129 (2004).

[62] U. C. Coskun, T.-C. Wei, S. Vishveshwara, P. M. Goldbart, A. Bezryadin, Science **304**, 1132 (2004).

[63] R. Saito, G. Dresselhaus, M. S. Dresselhaus, Phys. Rev. B **50**, 14698 (1994).

[64] A. Kanda, K. Tsukagoshi, S. Uryu, Y. Ootuka, Y. Aoyagi, Physica B **323**, 246 (2002).

[65] J.-O Lee, J.-R. Kim, J.-J. Kim, J. Kim, N. Kim, J. W. Park, K.-H. Yoo, K.-H. Park, Phys. Rev. B **61**, R16362 (2000).

[66] S. Roche, G. Dresselhaus, M. S. Dresselhaus, R. Saito, Phys. Rev. B **62**, 16092 (2000).

[67] S. Roche, R. Saito, Phys. Rev. B **59**, 5242 (1999).

Dank

An diese Stelle möchte ich allen danken, die auf verschiedenste Art und Weise zum Gelingen dieser Arbeit beigetragen haben. Dies sind u.a. all jene, die die Proben für mich hergestellt haben, die Messungen durchführten, die Daten auswerteten und mir die Ergebnisse erklärten.

Prof. Dr. Christoph Strunk danke ich herzlichst für all die Dinge, die ich bei und von ihm lernen durfte sowie für die Zeit, die er sich für all meine Anliegen nahm, auch wenn er keine hatte.
Martin "Magic" *Furtmeier* führte alle Konstruktionen, die sich bisher am Rande oder auch jenseits des bisher technisch Machbaren befanden, mit unglaublicher Geschwindigkeit und Präzision aus. Dafür mein aufrichtiger Dank.
Meinen Kollegen der ersten Stunde,*Andreas Bauer* und *Johannes Bentner*, möchte ich besonders danken. Sie erklärten mir große und kleine Geheimnisse der Probenherstellung und standen mir immer mit Rat und Tat zur Seite.
Wilfried Meindl danke ich neben vielem anderen für die angenehme Stimmung in unserem Büro.
Allen anderen Mitglieder des Lehrstuhls *Prof. Dr. Dieter Weiss* danke ich für Hilfe und Unterstützung in (fast) allen Lebenslagen und auch das positive Arbeitsklima.
Den Herrn *K. Weigert* und *B. Rother* danke ich dafür, dass Sie es doch immer wieder geschafft haben, der altersschwachen Verflüssigungsanlage doch noch genug Helium abzutrotzen.
Dr. Stephan Roche und *Dr. Francois Triozon* danke ich für die vielen Rechnungen und die fruchtbaren Diskussionen, ohne die große Teile dieser Arbeit nicht existeren würden.
Dr. Marc Buitelaar und *Prof. Dr. Christian Schönenberger* ließen mich in Basel an ihrem Know-How über Nanoröhren-Probenherstellung teilhaben. Dafür herzlichsten Dank.
Prof. Dr. Laszlo Forro und *Edina Ljubivic* stellten die besten Nanoröhren der Welt her und verschickten sie auch noch an uns. Danke!
Dr. Roland Schäfer und *Dr. Dinko Babic* danke ich für angenehme Zusammenarbeit und noch angenehmere unphysikalische Diskussionen und Ausflüge.
"Unseren" Forschungsstudenten *Christian Hagen*, *Christoph Hendlmeier* und *Keith Cobry* danke ich für die Tatkräftige Mithilfe bei Probenbau und Messung. Die Zusammenarbeit hat Spass gemacht und es kamen schöne Dinge dabei heraus!
"Meinem" Diplomanden *Lorenz Lechner* danke ich ebenfalls für die gute Zusammenarbeit. Er schaffte es in beängstigend kurzer Zeit, bessere Proben herzustellen als ich selbst.

All meinen Korrekturlesern danke ich für die Geduld, mein “Werk” zu lesen sowie für die nützlichen Anregungen zur Verbesserung.
Meine *Eltern* und meinem Bruder *Wolfgang* will ich für alle Unterstützung -auch die finanzielle- während des Studiums und auch noch jetzt danken.
Marion, ohne Dich hätte ich das alles nie geschafft. Danke, dass Du zu mir hältst, wir uns gegenseitig helfen und lieben.